2018

Probe of Electroweak Interference Effects in Non-Resonant Inelastic Electron-Proton Scattering

James Franklyn Dowd
College of William and Mary - Arts & Sciences, jfdowd001@gmail.com

Probe of Electroweak Interference Effects in Non-Resonant Inelastic Electron-Proton Scattering

James Franklyn Dowd
Yorktown, Virginia

Master of Science, College of William & Mary, 2011
Bachelor of Science, Virginia Polytechnic Institute & State University, 2009

A Dissertation presented to the Graduate Faculty
of The College of William & Mary in Candidacy for the
Degree of Doctor of Philosophy

Department of Physics

College of William & Mary
January 2019

APPROVAL PAGE

This Dissertation is submitted in partial fulfillment of
the requirements for the degree of

Doctor of Philosophy

James Franklyn Dowd

Approved by the Committee September 2018

Committee Chair
Chancellor Professor of Physics David Armstrong, Physics
College of William & Mary

Assistant Professor Wouter Deconinck, Physics
College of William & Mary

Professor of Physics Todd Averett, Physics
College of William & Mary

Dr. Mark Dalton, Staff Scientist
Thomas Jefferson National Accelerator Facility

Dr. Wally Melnitchouk, Staff Scientist
Thomas Jefferson National Accelerator Facility

ABSTRACT

The $\mathrm{Q}_{\mathrm{weak}}$ collaboration at Jefferson Lab made the first direct measurement of the proton's weak charge, Q_W^p, via a measurement of the parity-violating asymmetry in elastic $\vec{e}p$ scattering with low four-momentum transfer. To meet the high-precision goals, energy-dependent electroweak radiative corrections were applied to the measured asymmetry. The γZ box, $\Box_{\gamma Z}$, where a photon and a Z-boson are simultaneously exchanged, was the most problematic of these corrections. It could not be calculated through the same perturbative methods as the rest of the corrections. The $\Box_{\gamma Z}$ correction depends on theoretical models of the γZ interference structure functions, $F_{1,2}^{\gamma Z}$, for which there are almost no data.

Presented in this dissertation are the results from a specialized run of the $\mathrm{Q}_{\mathrm{weak}}$ experiment. Using the $\mathrm{Q}_{\mathrm{weak}}$ apparatus, with modifications, a measurement of the parity-violating asymmetry of non-resonant inelastic $\vec{e}p$ scattering was made with 3.35 GeV incident electrons. The apparatus was tuned to inelastic $\vec{e}p$ scattering with an average $W = 2.23\,\mathrm{GeV}$ and $Q^2 = 0.082\,\mathrm{GeV}^2$, in order to test the theoretical models used to predict the $\Box_{\gamma Z}$ radiative correction.

The final inelastic asymmetry, after correcting for beam polarization and backgrounds, was found to be $A_{Phys} = -13.5 \pm 4.4$ ppm, in agreement with theoretical predictions. This measurement provides important experimental validation of the theoretical methods used to calculate the $\Box_{\gamma Z}$ radiative correction. Additionally, this measurement provides useful experimental constraints on the $F_{1,2}^{\gamma Z}$ interference structure functions used in those theoretical models.

TABLE OF CONTENTS

ACKNOWLEDGEMENTS

First, I need to thank and acknowledge my sister, Dr. Melissa Dowd, M.D. Her unwavering dedication to self-improvement inspired me to go back to college in the first place. Without her support, championing, and often times outright nagging, I would not have started this journey. Her absolute confidence in me inspired the confidence I have in myself. I miss you Melissa and I wish you were still with us.

Another person who played a critical role in getting me to this point, is my undergraduate advisor, Mark Pitt. His early career advice was invaluable and helped me make up lost time as an older student. He sparked my interest in nuclear physics, introduced me to the Q_{weak} experiment, and recommended that I apply to William & Mary for graduate school.

I could not have asked for a better graduate advisor than David Armstrong. He is a brilliant and insightful teacher, with a keen ability to identify gaps in my knowledge and explain concepts at the precise level needed to help me bridge that gap myself. I am incredibly grateful for his support and all of the opportunities he has given me. I also want to thank David for his understanding when the balance between work and life was uneven. He's been more than just the head of my committee; he's been a true mentor.

I'd like to acknowledge and thank everyone on my committee: Wouter Deconinck, Todd Averett, Wally Melnitchouk, and Mark Dalton. Besides myself and David, Mark was the person most invested in my data set and acted as a second mentor. His guidance on which paths of analysis to further pursue and his own analysis on this data set were pivotal to the experiment. Wouter was my second advisor and deserves special recognition for his wealth of knowledge, advice on career development, and help with everything software related. I am also very appreciative of Wally and Todd for their helpful perspectives from outside of the Q_{weak} collaboration.

The Q_{weak} collaboration is comprised of a very large group with over a hundred collaborators, including professors, staff scientists, postdocs, grad students, and undergraduates. The precision of the Qweak result would not have been possible without the concerted effort of all these researchers and I am grateful for all of their contributions. I specifically want to thank Jay Benesch, Dave Gaskell, Jeong Han Lee, Dave Mack, Rob Mahurin, Katherine Mesick, and Greg Smith for their help and technical expertise. A special thanks to the ancillary physics group, in particular Mark Dalton, Mark Pitt, Anna Lee, and Steve Wells for their insight and feedback on my analysis.

All of my fellow graduate students, even if not named, deserve acknowledgement. I would like to thank Chris Triola for all of the late nights spent doing homework together and our lively debates.
Shout out to my fellow Hokie, Wade Duvall, who I've known since undergrad. His work on the database rootfiles, among other things, significantly reduced my analysis time.
Buddhini Waidyawansa, Rakitha Beminiwattha, and Scott MacEwan, thank you for being great office mates. There must have been something in the water for all of us to come out with Q_{weak} babies.
A special thanks is owed to Josh Magee for the back and forth banter and friendly antagonism, something at which he is so well adept, and for his enthusiastic support when I doubted myself. He has been a constant cheerleader.
Thank you to Juan Carlos Cornejo, my emergency exterminator. His ability to look at a page of code for no more than thirty seconds and find the bug never ceases to amaze me.
To the rest of my fellow William & Mary Q_{weak} group graduate students, including but not limited to Josh Hoskins, Kurtis Bartlett, Valerie Gray, and Victoria Owen. Thank you for your friendship and your constructive feedback each week.

Finally, I'd like to thank Brittany Dowd, my wife, my favorite debater, and my editor-in-chief. I am forever grateful for her love, support, and constant encouragement. I am humbled by the sacrifices she has made to her career in favor of my own and her unrelenting support of the pursuit of my career goals. I want to thank her for all of the late nights and red pens spent on editing my dissertation. This dissertation would not be what it is without her help.

I would also like to acknowledge my two children, Moira and Isaac. Without their help, I would have finished this much sooner.

Financial support for this research was provided by the National Science Foundation, under grants PHY-1068667, PHY-1405857, and PHY-1714792.

This work is dedicated

To my sister, Melissa

who inspired me to start grad school,

and

To my wife, Brittany

who made damn sure I finished.

LIST OF TABLES

LIST OF FIGURES

Chapter 1

Introduction

The experiment, described herein, was an ancillary measurement to the overall $\mathrm{Q}_{\mathrm{weak}}$ experiment. The $\mathrm{Q}_{\mathrm{weak}}$ experiment was a precision test of the Standard Model. The $\mathrm{Q}_{\mathrm{weak}}$ experiment determined the weak charge of the proton, Q_W^p, through a high precision measurement of the parity-violating asymmetry in elastic $\vec{e}p$ scattering [1]. The experiments were conducted at the Thomas Jefferson National Accelerator Facility in Newport News, VA. At the time, the accelerator facility had three experimental halls, which all shared the polarized electron beam.

The work described in this thesis was conducted during a two week period when a separate hall had beam priority. During this time, the kinematics of the beam were not conducive to the main $\mathrm{Q}_{\mathrm{weak}}$ experiment, as the hall was receiving the beam at a higher energy (3.35 GeV) than intended. This presented an opportunity to use the $\mathrm{Q}_{\mathrm{weak}}$ apparatus to make an important ancillary measurement.

At 3.35 GeV, the parity-violating inelastic asymmetry of $\vec{e}p$ scattering was determined in order to experimentally validate and constrain theoretical predictions of the $\mathrm{Re}\,\Box_{\gamma Z}^{V}$ correction to the weak charge of the proton and probe the $F_1^{\gamma Z}$, $F_2^{\gamma Z}$, and $F_3^{\gamma Z}$ interference structure functions.

1.1 $\mathbf{Q_{weak}}$ Experiment

The Standard Model of particle physics makes a robust prediction of the weak charge of the proton, $Q_W^p = 0.0708 \pm 0.0003$ [2]. The proton's weak charge defines the proton's interaction strength with other particles through the neutral electroweak force. Such definitively predicted observables of the Standard Model make great candidates for precision measurements, as a measured deviation could be a sign of new physics.

By exploiting parity-violation in the electroweak sector (see Sec. 2.2), the $\mathrm{Q_{weak}}$ experiment isolated the weak interaction to measure the weak charge of the proton, $Q_W^p = 0.0719 \pm 0.0045$ [1], in excellent agreement with the Standard Model value. The parity-violating elastic electron-proton scattering was precisely measured to have an asymmetry of $A_{ep} = -226.5 \pm 7.3$ (stat) $\pm$ 5.8 (syst) ppb. The total uncertainty achieved (9.3 ppb) provides a 4.1% measurement of the asymmetry.

To make such a precision measurement, any radiative corrections (see Sec. 2.3) must also be precisely known. One such correction to Q_W^p was the γZ box (see Sec. 2.3.1), which has considerable energy dependence [3]. The most recent calculations of the vector (0.0054 ± 0.0004) [4] and axial-vector (-0.0007 ± 0.0002) [5, 6] contributions were used, multiplied by a small Q^2 correction (0.978 ± 0.012) [7]. This corresponded to a $6.4\% \pm 0.6\%$ correction to Q_W^p. The total size of the γZ box correction, 0.0044, was comparable to the size of the uncertainty on Q_W^p, ± 0.0045. Therefore, a thorough understanding of the γZ box correction was vital.

The γZ box correction relies heavily on theoretical models of the γZ structure functions. The correction was known to sufficient precision for the $\mathrm{Q_{weak}}$ experiment [1], but that may not necessarily be the case for even more precise experiments in the future. Increasing the accuracy and precision of the γZ box theoretical predictions for the future will require inelastic scattering data over a wide range of kinematics, specifically scattering off of proton targets. The $\mathrm{Q_{weak}}$ inelastic data presented here is one such measurement.

Chapter 2

Motivation

2.1 The Standard Model

The Standard Model (SM) of particle physics is a unified relativistic quantum field theory based on the works of thousands of scientists over the past century. After decades of the cycle of experimental tests and theoretical predictions, the Standard Model has evolved to encompass and explain the known fundamental particles and their interactions, with the notable exception of gravity.

Fundamental particles in the Standard Model are divided broadly into two categories: bosons and fermions. Bosons are particles with integer spin. They are force carriers and mediate the interactions between particles. Fermions are particles with a 1/2 integer spin. The twelve fermions can be further subdivided into leptons and quarks, based on whether or not they interact with the strong force. Quarks are the constituent particles of protons, neutrons, and a variety of more exotic composite objects, while leptons include electron-like particles and their corresponding neutrinos.

Quarks and leptons are each categorized into pairs in three generations. The quark pairs, listed in order of increasing mass, are down & up, strange & charm, and bottom & top. The lepton generations, listed by increasing mass of the electron-like particle, are the electron & electron-neutrino, muon & muon-neutrino, and the tau & tau-neutrino.

Of the four fundamental forces in nature (electromagnetic force, strong force, weak force, and gravity), all but gravity are described by the Standard Model. These forces are mediated by the spin-1 bosons: photons, gluons, and Z^0 and $W^{\pm}$ bosons. The electromagnetic force is mediated by the massless photon. The strong force is mediated by eight massless gluons, which also bind quarks into hadrons. The weak force, most relevant to this research, is mediated by the massive Z^0 and $W^{\pm}$ bosons.

The fundamental symmetries in physics include charge, parity, time reversal, and Lorentz invariance. A symmetry is some physical or mathematical feature of a system that remains unchanged under a transformation of that system. For example, if you take a system and look at its mirror image, the physics in the mirror world will be the same as in the original system, if parity is a symmetry of the system. In such a case, parity is said to be 'conserved.' If parity is not a good symmetry of the system, parity is 'violated.'

As the name implies, the weak interaction is weaker than the electromagnetic interaction. As a consequence, the weak interaction is more difficult to measure. In the electromagnetic (EM) interaction, parity is conserved. However, in the weak interaction, parity is violated. Thus, examining the parity symmetry of a system allows the separation of weak interaction effects from EM interaction effects.

Isolating weak interactions allows the measurement of the strength of the weak interactions. This leads to a better understanding of the properties of the particles involved or within the interaction. Comparison of these measurements with predictions from the Standard Model, allows us to test the validity of the Standard Model. If a significant deviation from the Standard Model is observed, this could be an indication of new physics.

Certain limitations of the Standard Model are already known. In the originally formulated SM, neutrinos are predicted to be massless. However, neutrino oscillation experiments show that neutrinos have a non-zero mass and the original SM can be modified to accommodate massive neutrinos [8]. The SM also does not explain the matter-antimatter asymmetry in the universe [9] or the presence of dark matter and

dark energy [8]. Further, the SM does not account for gravity, overlooking one of the four fundamental forces of nature.

Richard Feynmann said "It doesn't matter how beautiful your theory is, it doesn't matter how smart you are. If it doesn't agree with experiment, it's wrong." We know that the Standard Model is wrong, or at least incomplete. Experiments, like the one described here, search for where theory deviates from reality, thus continuing the complementary cycle of evolving theory and experiments. This experiment tests theoretical predictions of a correction to the weak charge of the proton.

2.1.1 Fundamental Symmetries

The study of symmetries is fundamental to our understanding of physics, as they give insight into how the underlying physical process behaves. If the symmetry is not time or position dependent, it is considered a global symmetry. Otherwise, the symmetry is local. Newton's Laws [10] are examples of conservation of continuous global symmetries.

Global symmetries demonstrate the invariance of classical mechanics under a translation of time, position, or orientation. Emmy Noether showed that for any continuous global symmetry, there must be a corresponding conserved quantity [11]. For example, if a system is symmetric under a translation in position, then momentum is conserved. If, instead, a system is symmetric under a translation in time, then energy is conserved. The concept of conserved quantities can be extended to the quantum regime.

For example, the Dirac Lagrangian for a spin 1/2 particle (fermion) is

$$\mathcal{L} = \overline{\psi}\left(i\gamma^{\mu}\partial_{\mu} - m\right)\psi, \tag{2.1}$$

where m is the mass, γ^{μ} is the μ^{th} gamma matrix, and ψ is the wave function.

This Lagrangian is invariant under the addition of an arbitrary phase angle, α:

$$\psi \to e^{-iq\alpha}\psi. \tag{2.2}$$

This invariance is the simplest example of a gauge symmetry, and is known as a global gauge symmetry. In general, invariance of the Lagrangian results in the equations of motion for this particle remaining unchanged and specifically, the invariance with respect to the phase implies conservation of charge, q. If, instead, the gauge symmetry is time or position dependent, such as

$$\psi\left(x,t\right) \to e^{-iq\alpha(x,t)}\psi\left(x,t\right), \tag{2.3}$$

the resulting transformation becomes local rather than global. Under this local transformation, the Lagrangian, as given in Eqn. 2.1, is no longer invariant and the symmetry of the system is lost. To restore the invariance of the Lagrangian, a gauge field A_μ, with coupling g is introduced.

The derivative is replaced with the covariant derivative.

$$\partial_\mu \to \mathcal{D}_\mu \equiv \partial_\mu - iqA_\mu. \tag{2.4}$$

The gauge field itself transforms as

$$A_\mu \to A'_\mu = A_\mu + \frac{1}{q}\partial_\mu\alpha\left(x,t\right). \tag{2.5}$$

Requiring local invariance of the Lagrangian results in the addition of a vector gauge field, A_μ, with an associated particle called a gauge boson. This transformation is an example of $U(1)$ gauge invariance. In this case, the gauge boson introduced is the massless photon of the electromagnetic interaction.

2.2 The Electroweak Sector of the Standard Model

The Standard Model combines the strong, weak, and electromagnetic interactions in a $SU(3)_C \times SU(2)_L \times U(1)_Y$ gauge group, where C represents the color charge carried by quarks and gluons, L represents the preferentially 'left-handed' nature of the weak interaction, and Y is the weak hypercharge quantum number. A 'right-handed' particle is defined as a particle with its spin parallel to its momentum, and a 'left-handed' particle is defined as one with its spin anti-parallel to its momentum.

The $SU(2)_L \times U(1)_Y$ structure of the electroweak sector of the standard model unifies the electromagnetic and weak interactions. This gauge theory was developed by Glashow [12], Weinberg [13], and Salam [14], in the 1970's and has since been supported by experimental evidence.

No experimental observations of 'right-handed' neutrinos exist. Therefore, in the Standard Model, the 'left-handed' $SU(2)_L$ particles are defined in a doublet

$$\psi_L \equiv \begin{pmatrix} \psi_{\nu_e} \\ \psi_e \end{pmatrix}_L \tag{2.6}$$

and the 'right-handed' particles are defined in a singlet

$$\psi_R \equiv \psi_{eR}. \tag{2.7}$$

This leads to the 'left-handed' particles behaving differently than the 'right-handed' particles in the weak interaction. Thus, parity is violated in the weak sector.

2.2.1 Electroweak Unification

At high energies, the electromagnetic and weak forces are unified in the electroweak $SU(2)_L \times U(1)_Y$ guage theory . At lower energies, these forces diverge in a process known as spontaneous symmetry breaking.

Applying local gauge invariance (as discussed in Sec. 2.1.1) to the $SU(2)_L \times U(1)_Y$

electroweak gauge theory necessitates replacing the partial derivative ∂_μ with the covariant derivative $\mathcal{D}_\mu$. This covariant derivative is given by

$$\mathcal{D}_\mu = \partial_\mu + i\frac{g}{2}\tau^i W_\mu^i + i\frac{g'}{2}YB_\mu. \tag{2.8}$$

The weak isospin (I) invariance of the $SU(2)_L$ component introduces the three W_μ^i gauge particles, ($i = [1, 2, 3]$) with coupling strength g. The hypercharge invariance of the $U(1)_Y$ component introduces a single gauge particle B_μ with coupling strength g'. The Pauli matrices, τ^i, and weak hypercharge, Y, are known as the generators of the gauge groups. The electric charge, Q, comes about from a mixing of the generators, defined as

$$Q = I_3 + \frac{1}{2}Y \tag{2.9}$$

where I_3 is the third component of the weak isospin.

2.2.2 Spontaneous Symmetry Breaking

The physical gauge bosons, the massive $W^\pm$ and Z^0 and the massless photon, are consequences of the symmetry breaking of electroweak theory through the Higgs mechanism [15, 16]. When applying the Higgs mechanism and enforcing local gauge invariance, the relevant part of the Lagrangian is

$$\mathcal{L}_\phi = (\mathcal{D}_\mu\phi)^\dagger(\mathcal{D}^\mu\phi) - V(\phi^\dagger\phi) \tag{2.10}$$

where the potential $V(\phi^\dagger\phi)$ given by

$$V(\phi^\dagger\phi) = \mu^2\phi^\dagger\phi + \lambda(\phi^\dagger\phi). \tag{2.11}$$

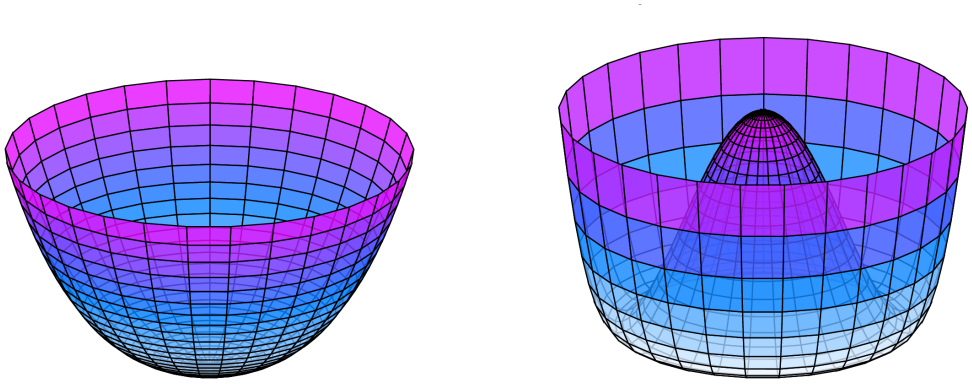

$\mu^2 > 0$ $\mu^2 < 0$

Figure 2.1: Diagram of the Higg's potential, simplified for illustrative purposes. The potential on the left, where $\mu^2 > 0$, is stable and has a single minimum at the center of the 'well'. The 'mexican-hat' potential on the right, where $\mu^2 < 0$, has infinite minima in the 'valley' surrounding the central peak.

This so-called 'mexican hat' potential has both quadratic and quartic dependence on the complex scalar doublet field ϕ, given by

$$\phi = \begin{pmatrix} \phi^+ \\ \phi^0 \end{pmatrix}. \tag{2.12}$$

The sign of the coefficient of the quadratic term determines whether the potential is stable or unstable (see Fig. 2.1). When $\mu^2 > 0$, the minima of the potential is at $\phi^\dagger\phi = 0$ and the potential is stable. This potential is unstable at $\phi^\dagger\phi = 0$ when $\mu^2 < 0$. The minima then becomes

$$\langle\phi\rangle^2 = \frac{\nu}{\sqrt{2}} \equiv \sqrt{\frac{\mu^2}{2\lambda}}, \tag{2.13}$$

where ν is the vacuum expectation value, or VEV. Making a choice for the VEV breaks the isospin symmetry resulting in the minimum of the potential to be

$$\phi = \frac{1}{\sqrt{2}} \begin{pmatrix} 0 \\ \nu \end{pmatrix}. \tag{2.14}$$

The covariant derivative in Eqn. 2.8 acting on this VEV,

$$\begin{aligned}\mathcal{D}_\mu\phi &= \frac{i}{2\sqrt{2}}\begin{pmatrix} gW_\mu^3 + g'B_\mu & g(W_\mu^1 - iW_\mu^2) \\ g(W_\mu^1 + iW_\mu^2) & -gW_\mu^3 + g^\mu \end{pmatrix}\begin{pmatrix} 0 \\ \nu \end{pmatrix} \\ &= \frac{i\nu}{2\sqrt{2}}\begin{pmatrix} g(W_\mu^1 - iW_\mu^2) \\ -gW_\mu^3 + g'B_\mu \end{pmatrix} \end{aligned} \tag{2.15}$$

can now be combined with the Lagrangian in Eqn. 2.10. The kinetic term of the Lagrangian becomes

$$\begin{aligned}(\mathcal{D}_\mu)^\dagger(\mathcal{D}^\mu) &= -\frac{g^2\nu^2}{4}W_\mu^+W^{\mu-} + \frac{\nu^2}{8}(-gW_\mu^3 + g'B_\mu)(-gW^{\mu 3} + g'B^\mu) \\ &= -\frac{g^2\nu^2}{4}W_\mu^+W^{\mu-} + \frac{\nu^2}{8}(g^2 + g'^2)Z_\mu Z^\mu + (0)A_\mu A^\mu, \end{aligned} \tag{2.16}$$

where the massless gauge fields, W_μ^i and B_μ, have been replaced using the following definitions of the physical gauge fields:

$$W_\mu^\pm = \frac{1}{\sqrt{2}}(W_\mu^1 \mp iW_\mu^2), \tag{2.17}$$

$$Z_\mu = \frac{gW_\mu^3 - g'B_\mu}{\sqrt{g^2 + g'^2}}, \tag{2.18}$$

$$A_\mu = \frac{gW_\mu^3 + g'B_\mu}{\sqrt{g^2 + g'^2}}. \tag{2.19}$$

The $W_\mu^\pm$, Z_μ, and A_μ fields represent the bosons in the weak charged-current interaction, the weak neutral interaction, and the electromagnetic interaction, respectively. The coefficients of these fields in Eqn. 2.16 yield the masses of these physical gauge bosons:

$$m_W = \frac{1}{2}\nu g, \tag{2.20}$$

$$m_Z = \frac{1}{2}\nu\sqrt{g^2 + g'^2}, \tag{2.21}$$

$$m_\gamma = 0. \tag{2.22}$$

The Fermi constant fixes the value of the VEV to be $\nu \approx 246\,\text{GeV}$ [2]. The predicted masses of the $W^{\pm}$ and Z^0 bosons show good agreement with the experimentally measured values of $m_W \approx 80.4\,\text{GeV}$ and $m_Z \approx 91.2\,\text{GeV}$ [2].

Examination of Equations 2.18 and 2.19 reveals that the observable A_μ and Z_μ fields are composed of different linear combinations of the original B_μ field and the third component of the W^i_μ field. This relationship can be rewritten in the form of a matrix transformation given by

$$\begin{pmatrix} Z_\mu \\ A_\mu \end{pmatrix} = \begin{pmatrix} \cos\theta_W & -\sin\theta_W \\ \sin\theta_W & \cos\theta_W \end{pmatrix} \begin{pmatrix} W^3_\mu \\ B_\mu \end{pmatrix} \tag{2.23}$$

where θ_W is the Weinberg angle (weak mixing angle) which characterizes the amount of mixing in electroweak theory. This is achieved using the following convenient angle parameterizations,

$$\tan^2\theta_W = \frac{g'^2}{g^2}, \tag{2.24}$$

$$\sin^2\theta_W = \frac{g'^2}{g^2 + g'^2}, \tag{2.25}$$

$$\cos^2\theta_W = \frac{g^2}{g^2 + g'^2}. \tag{2.26}$$

where the Weinberg angle is defined in terms of the coupling constants of the B_μ and W^i_μ fields. Both of the couplings, g and g', vary, or 'run,' with energy scale. Thus, the weak mixing angle, θ_W, will also 'run' with energy-scale.

2.2.3 Electroweak Neutral Current Interaction

The electroweak neutral current interaction can involve the exchange of either of the two neutrally charged bosons in the theory: the γ or the Z^0, shown in Fig. 2.2.

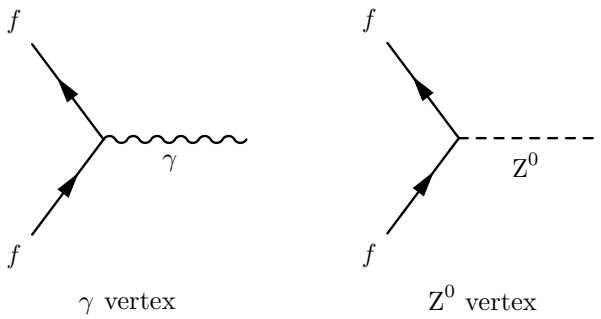

Figure 2.2: Neutral current exchange diagrams for the electromagnetic (left) and neutral-weak (right) interactions.

The associated neutral currents for these exchanges are

$$J_\mu^\gamma = Q\bar{\psi}\gamma_\mu\psi, \tag{2.27}$$

$$J_\mu^{Z^0} = J_\mu^3 \cos\theta_W - J_\mu^Y \sin\theta_W, \tag{2.28}$$

where γ_μ is the μ^{th} Dirac gamma matrix. The J_μ^3 and J_μ^Y currents correspond to the W_μ^3 and B_μ fields respectively. In terms of the fermion fields and the couplings, these currents are

$$J_\mu^Y = \frac{1}{2}g'Y\bar{\psi}\gamma_\mu\psi, \tag{2.29}$$

$$J_\mu^3 = -\frac{1}{2}g\bar{\psi}_L\gamma_\mu\psi_L. \tag{2.30}$$

Eqn. 2.28 can be formulated in terms of the fermion fields and their couplings. This expanded equation takes the following form

$$J_\mu^{Z^0} = \frac{1}{2}g_Z\Big([2I_3 - 2Q\sin^2\theta_W]\bar{\psi}_L\gamma_\mu\psi_L + [-2Q\sin^2{}_W]\bar{\psi}_R\gamma_\mu\psi_R\Big), \tag{2.31}$$

where the Z^0 coupling constant, g_Z, is given by

$$g_Z = \frac{e}{\sin\theta_W\cos\theta_W}. \tag{2.32}$$

Rewritten in a much more compact form, Eqn. 2.28 becomes

$$J_{\mu}^{Z^0} = \bar{\psi}\gamma_{\mu}(g_V - g_A\gamma^5)\psi, \tag{2.33}$$

with the introduction of a weak vector fermion coupling, g_V, and a weak axial-vector fermion coupling, g_A. These couplings are defined as

$$g_V \equiv I_3 - 2Q\sin^2\theta_W, \tag{2.34}$$

$$g_A \equiv I_3. \tag{2.35}$$

In terms of these two new couplings and the electromagnetic charge, Q, the vertex factors for the exchanges in Fig. 2.2 are

$$Z^0 : \ -\frac{i}{2}g_Z\gamma_{\mu}(g_V - g_A\gamma^5), \qquad \gamma : \ -ieQ\gamma_{\mu}. \tag{2.36}$$

Analogous to the electromagnetic charge, the weak vector charge is given by g_V and the weak axial charge is given by g_A. Values for all three of these charges for the fundamental fermions plus the third component of weak isospin, I_3, are summarized in Tab. 2.1.

Particle	Q	I_3	$2g_V$	$2g_A$
u, c, t	$+\frac{2}{3}$	$+\frac{1}{2}$	$1 - \frac{8}{3}\sin^2\theta_W$	$+1$
d, s, b	$-\frac{1}{3}$	$-\frac{1}{2}$	$-1 + \frac{4}{3}\sin^2\theta_W$	-1
ν_e, ν_μ, ν_τ	0	$+\frac{1}{2}$	$+1$	$+1$
e^-, μ^-, τ^-	-1	$-\frac{1}{2}$	$-1 + 4\sin^2\theta_W$	-1

Table 2.1: The SM values for the electromagnetic charge (Q), third component of the weak isospin (I_3), and the vector and axial coupling for the quarks and leptons.

With the appropriate combination of quark contributions, the weak charges of the

proton (uud) and neutron (udd), at tree level are

$$Q_W^p = 1 - 4\sin^2\theta_W, \tag{2.37}$$

$$Q_W^n = -1. \tag{2.38}$$

To leading order, the neutral-weak scattering amplitudes of the Z^0 and γ are proportional to the following propagators

$$Z^0 : \ \frac{-i(g_{\mu\nu} - q_\mu q_\nu / M_Z^2)}{q^2 - M_Z^2}, \qquad \gamma : \ \frac{ig_{\mu\nu}}{q^2} \tag{2.39}$$

where q_μ is the four-momentum of the exchanged boson and $g_{\mu\nu}$ is the metric tensor. In the limit where $q^2 \ll M_Z^2$ (the regime of low energy experiments), the propagator for the Z^0 exchange reduces to a short-ranged four-point contact interaction given by

$$\frac{ig_{\mu\nu}}{M_Z^2}. \tag{2.40}$$

2.3 Radiative Corrections to the Proton's Weak Charge

Thus far, only single boson exchanges have been considered. This is known as the Born approximation. Radiative corrections, in the context of the weak charge of the proton, are modifications of the Born approximation that arise when higher order Feynman diagrams are included in calculations of the scattering cross section.

These higher-order multiple boson diagrams include both electromagnetic and electroweak interactions. Electromagnetic radiative corrections can be either internal or external and can involve both real and virtual photon exchanges. External corrections primarily arise from emission of a 'hard' photon as a charged particle enters the field of a nucleus, in a process called bremsstrahlung radiation.

Loops of virtual photons and fermions result in higher-order internal electromagnetic corrections. Figure 2.3 shows the Feynman diagrams of some example internal electromagnetic corrections.

Internal and external electromagnetic corrections will alter the cross section, asymmetry, and kinematics of the interaction. For more information on these types of radiative corrections, see [17] and [18].

Additional diagrams involving the exchange of the $W^{\pm}$ and Z^0 weak bosons are called the electroweak radiative corrections. The electroweak corrections can manifest in a form similar to the electromagnetic corrections; an important class of these are the 'box' diagrams (see Fig. 2.4).

At tree level, the weak charge of the proton, Q_W^p, is related to the weak mixing angle, $\sin^2\theta_W$, by the following equation:

$$Q_W^p = 1 - 4\sin^2\theta_W \tag{2.41}$$

constructed by adding the appropriate combination of quark weak vector charges based on the quark content of a proton (u + u + d). Tree level knowledge of Q_W^p was insufficient for the precision goals of the Q_{weak} experiment. It was necessary to examine the proton's weak charge further and include electroweak radiative corrections, which can be written as [3]

$$Q_W^p = \left(1 + \Delta_\rho + \Delta_e\right)\left(1 - 4\sin^2\theta_W(0) + \Delta_e'\right) + \Box_{WW} + \Box_{ZZ} + \Box_{\gamma Z}(0), \tag{2.42}$$

where Δ_ρ is a vacuum polarization correction, Δ_e is a vertex correction to the γe vertex, Δ_e' is a vertex correction to the Ze vertex, and $\Box_{WW}$, $\Box_{ZZ}$, and $\Box_{\gamma Z}$ are corrections for two-boson exchange interactions (See Fig. 2.4).

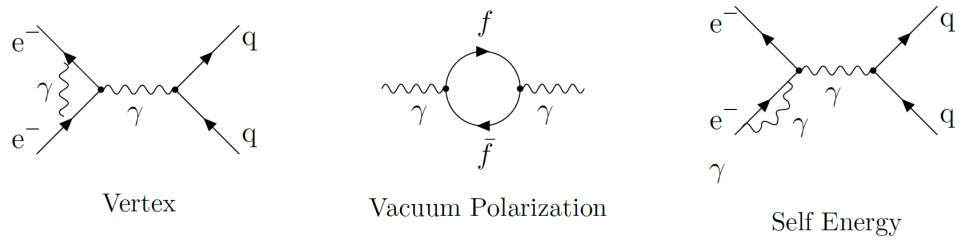

Figure 2.3: Example Feynman diagrams illustrating next-to-leading order corrections.

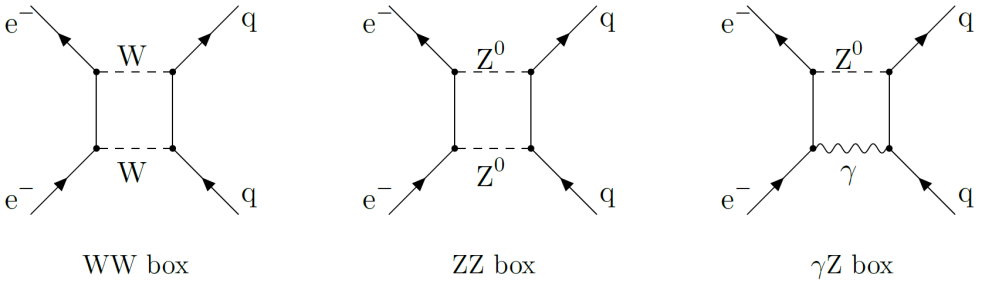

Figure 2.4: Feynman diagrams for the WW box (left), ZZ box (center), and the γZ box (right) are shown.

The correction terms Δ_ρ, Δ_e, and Δ_e' have been examined in detail in Ref. [3]. Using perturbative Quantum Chromodynamics (pQCD), both the $\Box_{WW}$ and $\Box_{ZZ}$ can be calculated to high precision due to the large masses of the $W^\pm$ and Z^0 bosons, which make them short range effects [19–21]. Recall from Equation 2.40 that the propagator for the exchange of a Z-boson scales as $\frac{1}{M_Z^2}$. The final correction, $\Box_{\gamma Z}$, is more problematic to calculate because it contains competing short and long range effects.

2.3.1 Theoretical Predictions of the γZ Box

Until recently, the $\Box_{\gamma Z}$ correction was thought to be known well enough for the precision requirements of the Q_{weak} measurement. However, in 2009, Gorchtein and Horowitz [22] demonstrated that the $\Box_{\gamma Z}$ term was much larger at Q_{weak} energies than previously estimated [3] and had a strong energy dependence (see Fig. 2.5). This lead to further development of models of the $\Box_{\gamma Z}$ contribution to Q_W^p by several groups [4, 7, 23–25] (See Tab.2.2).

Ultimately, the main Q_{weak} experiment adopted the most recent calculations [1] for both the vector [4] and axial-vector [5, 6] components of $\Box_{\gamma Z}$.

Only an overview of the key points in the theoretical examination of $\Box_{\gamma Z}$ will be explored here, and the discussion will follow Hall *et al.* [4, 25].

The γZ-Box correction can be defined in terms of the electroweak scattering

Correction	Value	Reference
$\mathrm{Re}\,\Box^V_{\gamma Z}$	$(5.4 \pm 2.0) \times 10^{-3}$	[7]
	$(4.7^{+1.1}_{-0.4}) \times 10^{-3}$	[23]
	$(5.7 \pm 0.9) \times 10^{-3}$	[24]
	$(5.4 \pm 0.4) \times 10^{-3}$	[4]
$\mathrm{Re}\,\Box^A_{\gamma Z}$	$(3.7 \pm 0.4) \times 10^{-3}$	[5]
	$(4.0 \pm 0.5) \times 10^{-3}$	[24]

Table 2.2: Theoretical predictions of both the vector and axial-vector components of $\Box_{\gamma Z}$ evaluated at the energy of the main $\mathrm{Q}_{\mathrm{weak}}$ experiment ($E = 1.165\mathrm{GeV}$).

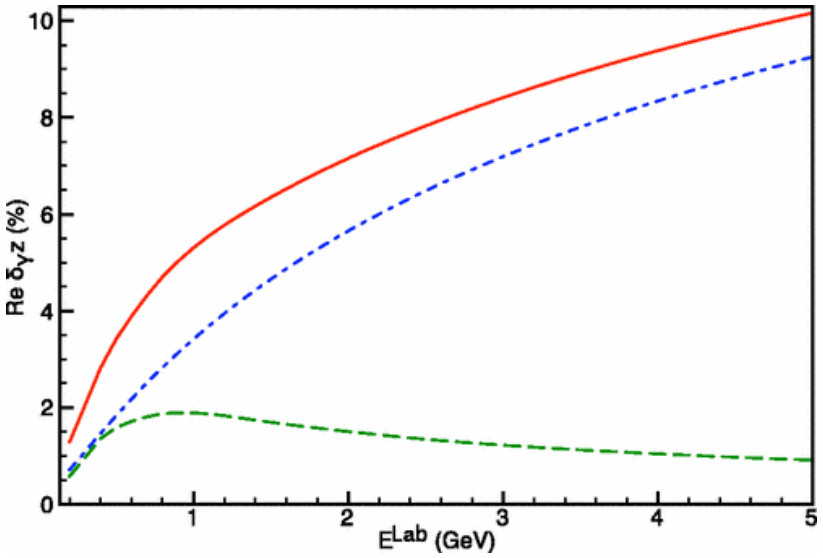

Figure 2.5: Gorchtein and Horowitz's results showing the energy dependence of $\mathrm{Re}\,\delta_{\gamma Z_A}$ ($\Box^A_{\gamma Z}$). The two pieces of their integral calculations over the γZ structure functions are shown (Blue dot-dashed curve and green dashed curve). The total correction is the solid red curve. Recall that the beam energy for the main $\mathrm{Q}_{\mathrm{weak}}$ measurement was 1.15 GeV. Reproduced from [22].

amplitudes as [26]

$$\Box_{\gamma Z}(0) = Q_W^p \frac{\mathrm{Re}(\mathcal{M}^*_\gamma \mathcal{M}^{PV}_{\gamma Z})}{\mathrm{Re}(\mathcal{M}^*_\gamma \mathcal{M}^{PV}_{Z})}. \tag{2.43}$$

Here, $\mathcal{M}_\gamma$ is the electromagnetic Born amplitude, $\mathcal{M}^{PV}_Z$ is the parity-violating component of the Born Z exchange amplitude, and $\mathcal{M}^{PV}_{\gamma Z}$ is the parity-violating component of the γZ interference amplitude.

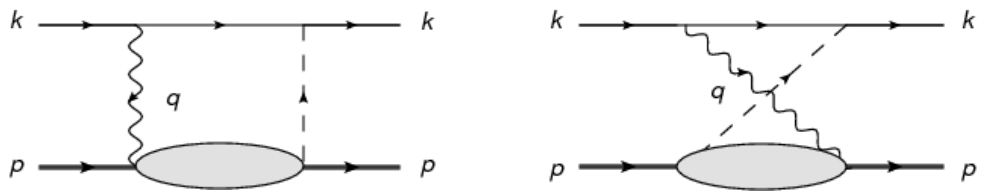

Figure 2.6: γZ box (left) and crossed-box (right) diagrams include the on shell intermediate excited states of the proton (elipses). The incoming electron and target proton are represented by the thin and thick black lines, respectively. The virtual photon and Z-boson exchanged are represented by the curvy and dashed lines, respectively. Reproduced from [25].

The γZ-Box interference correction can be separated into two parts:

$$\Box_{\gamma Z}(E) = \Box^{A}_{\gamma Z}(E) + \Box^{V}_{\gamma Z}(E) \tag{2.44}$$

The term $\Box^{A}_{\gamma Z}$ is the part arising from the electron vector with hadronic axial-vector coupling to the Z-boson, and the term $\Box^{V}_{\gamma Z}$ is the part arising from the electron axial-vector with hadronic vector coupling to the Z-boson. The $\Box^{V}_{\gamma Z}$ term dominates the energy dependence of the overall correction and has a much larger uncertainty. Therefore, $\Box^{V}_{\gamma Z}$ will be the focus going forward. For details on the $\Box^{A}_{\gamma Z}$ component, consult [5, 6, 19, 20].

The hadronic structure dependent contributions from the box diagrams are the primary challenge to calculating these radiative corrections [22]. These hadronic structure dependent contributions require an inclusive sum over excited intermediate states, calculated using a dispersion relation (see Fig. 2.6).

For the real part of $\Box^{V}_{\gamma Z}$ and for forward inelastic scattering, the dispersion relation is given by

$$\mathrm{Re}\,\Box^{V}_{\gamma Z}(E) = \frac{2E}{\pi}\mathcal{P}\int_0^\infty dE' \frac{1}{E'^2 - E^2}\,\mathrm{Im}\,\Box^{V}_{\gamma Z}(E'), \tag{2.45}$$

where $\mathcal{P}$ is the principal value integral.

Using the optical theorem, the imaginary part of the parity-violating amplitude for

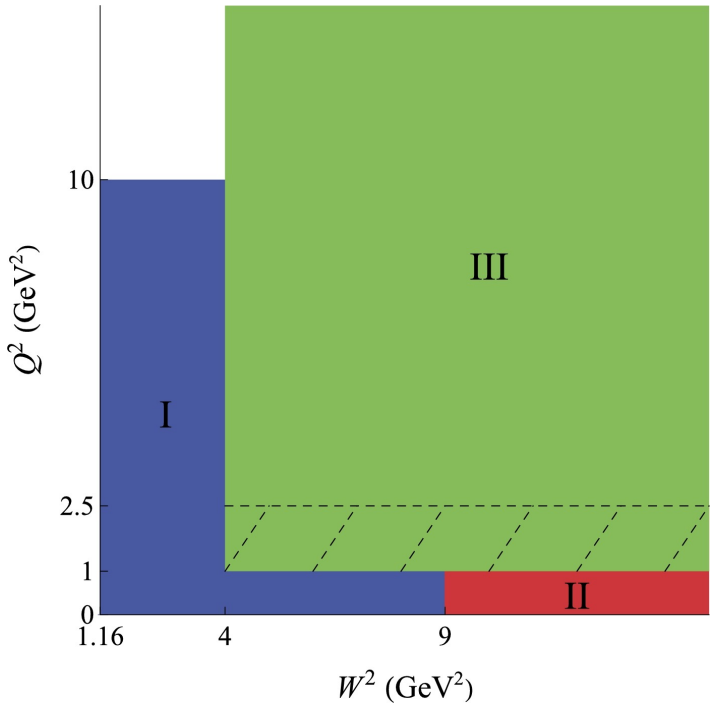

Figure 2.7: Break down of the three kinematic regions that contribute to $\Box_{\gamma Z}^{V}$ integrals. With $W^2 = 5.0\,\mathrm{GeV}^2$ and $Q^2 = 0.075\,\mathrm{GeV}^2$, the results of this experiment will reside in Region I. Reproduced from [4].

γZ exchange can be written as

$$2\,\mathrm{Im}\,\mathcal{M}_{\gamma Z}^{(PV)} = -4\sqrt{2}\pi M G_F \int \frac{d^3k'}{(2\pi)^3 2E_{k'}} \left(\frac{4\pi\alpha}{Q^2}\right)\left(\frac{1}{1+Q^2/M_Z^2}\right) L_{\mu\nu}^{\gamma Z} W_{\mu\nu}^{\gamma Z}, \quad (2.46)$$

where $Q^2 = -q^2$ is the four-momentum transfer of the exchange boson, $k' = k - q$ is the integration variable, and $L_{\mu\nu}^{\gamma Z}$ and $W_{\mu\nu}^{\gamma Z}$ are the γZ lepton tensor and nucleon initial state hadronic tensor, respectively. The hadronic tensor can be expressed in terms of the γZ interference structure functions as

$$MW_{\gamma Z}^{\mu\nu} = -g^{\mu\nu} F_1^{\gamma Z} + \frac{p^\mu p^\nu}{p\cdot q} F_2^{\gamma Z} - i\epsilon^{\mu\nu\lambda\rho}\frac{p_\lambda q_\rho}{2p\cdot q} F_3^{\gamma Z}, \quad (2.47)$$

where p is the target hadron's four-momentum. The $F_1^{\gamma Z}$ and $F_2^{\gamma Z}$ structure functions both contribute to $\Box_{\gamma Z}^{V}$, and the $F_3^{\gamma Z}$ structure function contributes to $\Box_{\gamma Z}^{A}$.

These structure functions are functions of two kinematic variables: either Q^2 and

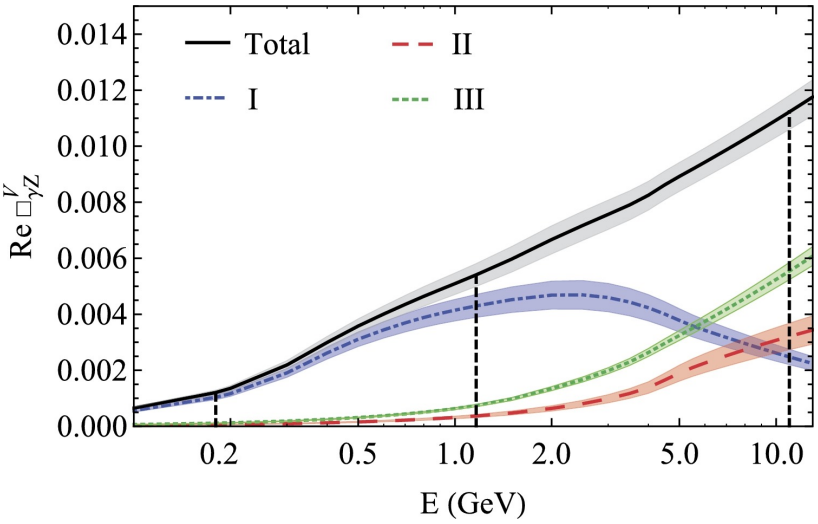

Figure 2.8: The energy dependence of the total $\Box_{\gamma Z}^{V}$ correction (black solid line) is separated into the contributions from the three integration regions in Fig. 2.7, Region I (blue dot dashed line), Region II (red dashed line), and Region III (green dotted line). The vertical dashed lines at $E = 0.18\,\text{GeV}$, $E = 1.165\,\text{GeV}$, and $E = 11\,\text{GeV}$ indicate the beam energies of the MESA [27], Q_{weak} [1], and MOLLER [28] PV experiments, respectively. Reproduced from [4].

Bjorken $x = Q^2/2p \cdot q$, or Q^2 and W^2. Combining Eqn. 2.46 and Eqn. 2.47 results in integrals over these kinematic variables. These integrals can be broken up into three separate integration regions, in terms of W^2 and Q^2 (see Fig. 2.7). The γZ structure functions are parameterized using different models for each region.

In contrast to the electromagnetic structure functions, which have a plethora of data available, the γZ structure functions are not well determined experimentally (see Sec. 2.3.2). As a consequence, the γZ structure functions must be expressed using models. In particular, there is little or no information available for the low W and low Q^2 region [25] (Region I of Fig. 2.7). Region I dominated the $\Box_{\gamma Z}$ correction applied to the main Q_{weak} measurement and its uncertainty (see Fig. 2.8). With $W = 2.23\,\text{GeV}$ and $Q^2 = 0.082\,\text{GeV}^2$, the Q_{weak} inelastic PV asymmetry measurement presented here, lies in Region I. This presents an excellent opportunity to experimentally test these models. A prediction of that inelastic asymmetry at the Q_{weak} inelastic beam energy ($E = 3.35\text{GeV}$) is provided in Ref. [25] and is reproduced with modifications in Sec. 5.1.4.

2.3.2 Previous Experimental Constraints

The G^0 [29] and E08-011 (PVDIS) [30, 31] experiments at Jefferson Lab provided previous experimental input for γZ-box calculations. Like this measurement, both experiments measured parity-violating inelastic electron scattering, but at different kinematics. The Q_{weak} inelastic scattering asymmetry data was measured at a much lower $Q^2 = 0.082$ GeV than either the G^0 or E08-011 (PVDIS) experiments.

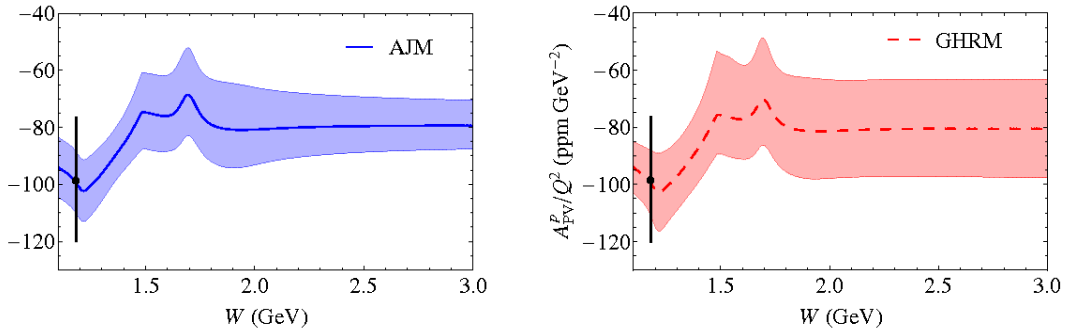

Figure 2.9: Theoretical predictions of the reduced parity-violating asymmetry, A_{PV}/Q^2, plotted as a function of W. The left plot is the AJM model prediction and the right is the GHRM model prediction. The incident energy $E = 0.69$ GeV, and $Q^2 = 0.34$ GeV^2 are fixed. The G^0 results (black circle) have $W = 1.18$ GeV. Reproduced from [25].

The G^0 experiment measured the parity-violating inelastic asymmetry of electron-proton scattering at a backward angle, whereas Q_{weak} measured forward scattering. With beam energy, $E = 0.69$ GeV, and $Q^2 = 0.34$ GeV^2, the kinematics of this experiment were near the Delta resonance. The asymmetries predicted by the AJM and GHRM models at the G^0 kinematics are shown in Fig. 2.9. The central value of the data agrees with both models, providing experimental validation at these kinematics, but the uncertainty of the data is too large to significantly constrain the γZ structure functions [25].

The E08-011 experiment measured the asymmetry of electron-deuteron Parity-Violating Deep Inelastic Scattering (PVDIS) in both the resonance region and the Deep Inelastic Scattering (DIS) region. The asymmetry was measured at two beam energies, $E = 4.9$ GeV and $E = 6.1$ GeV, over a wide range of W and Q^2. The resonance region data has been analyzed (see Fig. 2.10) and has already been used

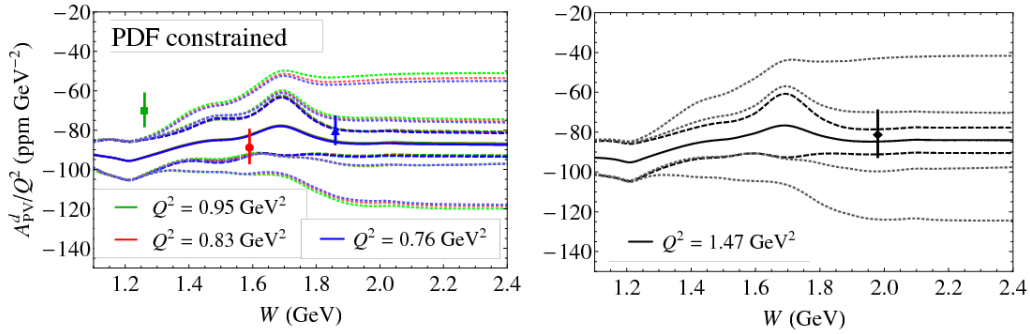

Figure 2.10: Theoretical predictions of the reduced parity-violating asymmetry, A_{PV}/Q^2, plotted as a function of W, at the two beam energies of the PVDIS experiment, $E = 4.9$ GeV (left plot) and $E = 6.1$ GeV (right plot). The data points at $W = 1.26$ (green square), 1.59 (red circle), 1.86 (blue triangle) and 1.98 GeV (black diamond) correspond to average values of $Q^2 = 0.95$, 0.83, 0.76 and 1.47 GeV^2, respectively. Each of the four data points above are averaged values from a range of W and Q^2 data points. Reproduced from [25].

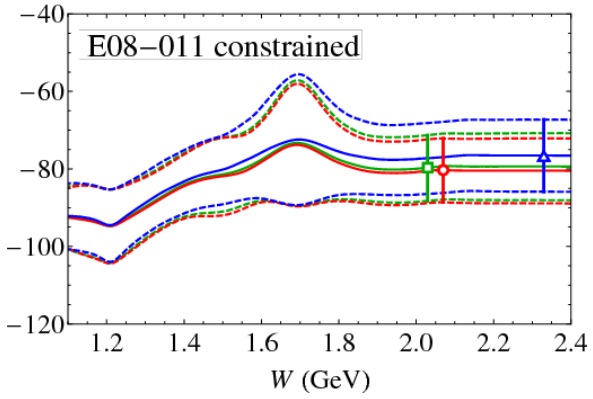

Figure 2.11: Theoretical predictions for the reduced parity-violating deuteron asymmetry, A_{PV}/Q^2, plotted as a function of W for the DIS region kinematics of the PVDIS data. The predictions at the experimental W values with $Q^2 = 1.28$ GeV^2 (green square), 1.09 GeV^2 (red circle) and 1.90 GeV^2 (blue triangle) are psudo-data points and do not represent the measured asymmetries. Reproduced from [25].

to constrain the γZ structure functions used in the AJM model [25]. The analysis of the PVDIS data in the DIS region has not been completed yet. Fig. 2.11 shows the predicted asymmetries for the DIS region PVDIS data using the AJM model with constraints from the resonance region data.

Chapter 3

Experimental Apparatus

The entire Q_{weak} apparatus is described in detail in the article, *The Qweak experimental apparatus* [32]. Here, I will give brief descriptions of key subsystems of the apparatus, focusing primarily on where the experimental setup in the present work differed from the main Q_{weak} measurement [1, 33].

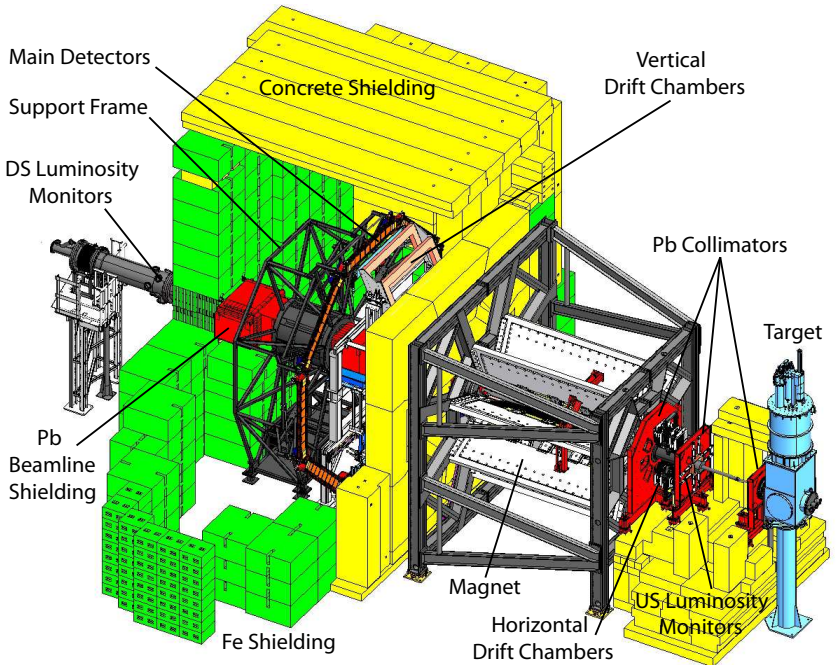

Figure 3.1: Schematic showing the Q_{weak} apparatus. Reproduced from [32].

3.1 Electron Beam Accelerator

Thomas Jefferson National Accelerator Facility (Jefferson Lab) in Newport News, Virginia, is host to the Continuous Electron Beam Accelerator Facility (CEBAF) with four experiment halls. The research described in this work was conducted before the addition of the fourth experiment hall, and before the accelerator's maximum beam energy was increased from 6 GeV to 12 GeV [34]. The relevant components of the accelerator are the polarized source, spin-rotators, pre-accelerator, injector, and two linear accelerators (LINACs)[32].

The polarized source provides the polarized electrons. The injector accelerates the beam to relativistic velocities synchronized with the LINACs. The electrons enter the first LINAC with an energy of 62 MeV. Each LINAC accelerated the beam by 548 MeV. The LINACs are joined by recirculating arcs that allow for one to five passes around the accelerator. The accelerator was capable of delivering polarized beam to the three experiment halls simultaneously, but no two halls could receive beam from the same pass around the accelerator.

For the measurement presented here, the Q_{weak} apparatus in Hall C received polarized electrons after 3 passes, resulting in a beam energy of 3.35 GeV.

For a thorough description of the components and capabilities of the Jefferson Laboratory accelerator, see Ref. [35].

3.1.1 Fast Helicity Reversal

Helicity reversal is a process by which the spin of the beam electrons is alternated to be either aligned (+) or anti-aligned (-) with the electron's momentum vector. The helicity of the electron beam was reversed at 960 Hz, with a pseudo-randomized pattern of either '$-++-$' or '$+--+$'. These quartet patterns were used to remove the effect of any linear drifts in the detector signals.

The yields for each detector photo-multiplier tube (PMT) are integrated over each helicity state. Yield is defined as the PMT voltage divided by the beam current.

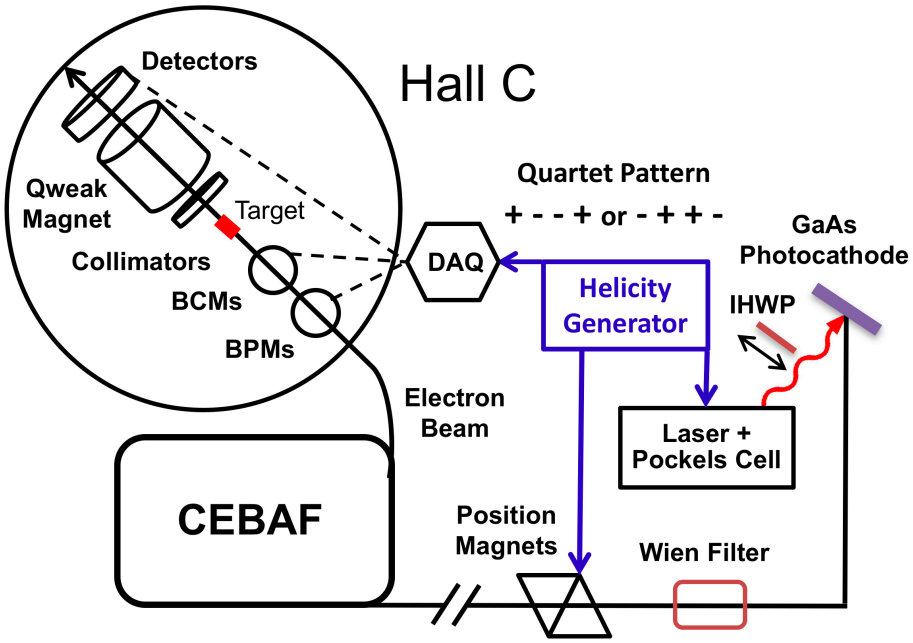

Figure 3.2: Schematic of the electron beam source of the CEBAF accelerator and Experimental Hall C, at Jefferson Lab in Newport News, Virginia. Reproduced from [36].

The raw asymmetry, A_{raw}, is measured for each helicity quartet with the following equation:

$$A_{raw} = \frac{Y^+ - Y^-}{Y^+ + Y^-} \tag{3.1}$$

where $Y^{\pm}$ is the integrated PMT signal yield for a right-handed/left-handed ($\pm$) helicity state [32].

3.1.2 Monitoring and Manipulation

After approximately every eight hour period of data collection, an insertable half-wave plate (IHWP) was either inserted or retracted from the path of the linearly polarized light in the polarized beam source (see Fig. 3.2). This changed the relative sign of the linearly polarized light to the circularly polarized light before it produced polarized electrons by striking the photocathode. Study of the effect of this "slow" non-electronic helicity reversal was used to understand and cancel helicity-correlated beam properties, or properties of the beam that vary with helicity state.

The experiment utilized a second "slow" helicity reversal based on a two-Wien spin flipper consisting of a vertical Wien filter, followed by two solenoid magnets, and a horizontal Wien filter [37]. The system is designed such that, by reversing the current in the solenoids, the polarization of the electron beam is reversed, while maintaining the optical focusing properties of the system. This provides a systematic check of the correlation between the helicity of the laser and the photo-produced electrons, while cancelling certain kinds of false asymmetries. For the 'main' Q_{weak} measurement, the two-Wien system was changed monthly. The data for the current analysis were collected within a single period of this "slow" helicity reversal.

The beam current was measured continuously and non-invasively using six RF cavity Beam Current Monitors (BCMs) upstream of the target. Beam position and angle at the target were determined using a combination of Beam Position Monitors (BPMs) upstream of the target. The position and angle of the beam was continuously monitored and recorded by a series of BPMs, with 24 BPMs in the injector beamline and 23 BPMs in the Hall C beamline.

3.1.3 Beam Polarimetry

The electron beam polarization was measured using two independent polarimeters. Having two polarimeters allowed cross checking of this measurement [38].

An existing Møller polarimeter in Hall C [39] was only used periodically, because the measurement was invasive and required beam currents much lower than those employed by the experiment. The Møller polarimeter utilized a thin iron target placed perpendicular to the beam axis. The iron was polarized parallel to the beam axis using a solenoid magnet. Electrons from the beam scattered off the polarized electrons in the iron (see Fig. 3.3). The scattered and recoil electrons were focused onto two detectors using quadrupole magnets, where their asymmetries were measured.

Additionally, a non-invasive Compton polarimeter provided continuous polarization measurements [40] (see Fig. 3.4). The polarized electron beam was diverted by a magnetic chicane to a laser table. Here the electrons interacted with circularly polarized

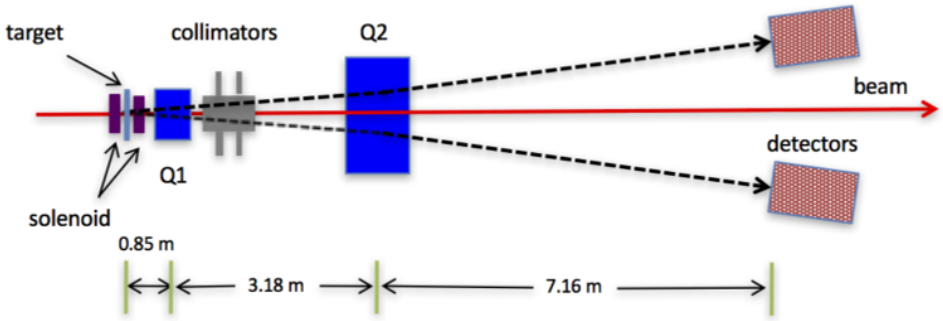

Figure 3.3: Schematic of the Møller polarimeter. The red line shows the electron beam entering from the left. The dashed black line are the scattered and recoil electrons. $Q1$ and $Q2$ are the quadrupole magnets.

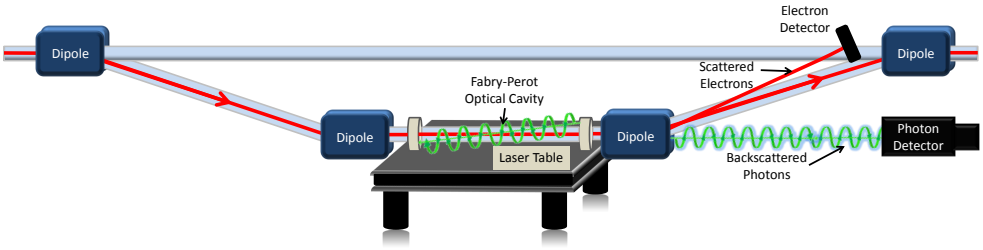

Figure 3.4: Schematic of the Compton polarimeter. The red line shows the electron beam entering from the left and traversing the chicane. Circularly polarized photons are indicated by the green lines. Reproduced from [32].

photons. The scattered electron and the back-scattered photon were detected in a diamond strip electron detector and a calorimeter, respectively. The unscattered beam progressed through the rest of the chicane, back to the beam pipe, and ultimately continued to the target.

3.2 Target

3.2.1 Liquid Hydrogen Target

The main Q_{weak} target consisted of a closed loop of $\sim$58 L of unpolarized liquid hydrogen (ℓH_2) re-circulated by a pump, a heat exchanger to liquify the hydrogen and remove the heat deposited by the beam, an aluminum vessel where the electron beam

interacted with the hydrogen, and a heater to both regulate the temperature of the hydrogen and to replace the beam power when the beam was off [32].

The incoming electron beam first encountered the entrance window of the target vessel. Scattering from the window was an undesirable background. To minimize scattering, the entrance window was machined as thin as possible (0.097 mm thick Al 7075-T6), while maintaining safety. The ℓH_2 interaction region was contained in a conical Al vessel oriented along the beam axis to accommodate all scattered electrons in the experiment's angular acceptance, $5.8^\circ < \theta < 11.6^\circ$.

The Q_{weak} target was designed to be long, 34.4 cm, or 3.9% radiation lengths, to enhance the number of scattering events per unit volume of ℓH_2. Scattered electrons pass through the large diameter exit window (0.64 mm thick Al 7075-T6). Unscattered electrons pass through the thinner center (0.125 mm thick) of the exit window. Electrons which scattered from either Al target window were a source of background to the asymmetry measurement.

The target vessel was designed using computational fluid dynamics (CFD) to maximize the flow of ℓH_2 transversely across the beam axis and thereby minimize density fluctuations and target boiling. The incident beam was rastered in a square pattern, typically 4 mm per side, to avoid depositing excessive heat on a single spot on the target entrance window and to reduce the effects of target boiling.

3.2.2 Solid Targets

In addition to Q_{weak}'s primary hydrogen target, there was also an array of solid targets which were used for various systematic studies. The important solid targets used in this measurement were a series of Al solid targets machined from the same Al alloy as the Al target windows. These Al targets were used to determine the effect of the Al target windows on the measured asymmetry.

3.3 Toroidal Magnet Spectrometer

The Q_{weak} toroidal magnetic spectrometer (QTor) bent the trajectory of scattered particles to select a specific energy or momentum range. QTor was centered 6.5 m downstream of the target center. It consisted of eight copper coils arrayed azimuthally about the beamline. The frames holding the coils in place were constructed out of aluminum to minimize magnetic material near the magnet.

The magnetic coils were arranged about the beam axis and oriented between holes of the collimators (see Sec. 3.5). This configuration prevented secondary scattering off the magnetic coils.

The system was designed to focus elastically scattered electrons from a ∼1.1 GeV beam onto the main detectors. With a beam energy of 3.35 GeV, both inelastically and highly radiated elastically scattered electrons, as well as pions mostly from photoproduction, are directed into the acceptance of the apparatus. Low-energy electrons from Møller scattering are swept radially away and out of the experiment's acceptance by the magnetic field.

3.4 Main Detectors

The experiment's main detectors consisted of eight fused silica Cherenkov detectors placed symmetrically about the beam axis. Each detector consisted of two 100 cm long quartz bars connected by an optical glue joint in the middle. Two Photo-Multiplier Tubes (PMTs) were glued to the detector, with one at each end. The total active area of each detector was 200 cm × 18 cm, so the entire array covered 49% of 2π in azimuthal angle [32].

Charged particles passing through the bar generated optical photons via the Cherenkov effect, which propagated inside the quartz to the PMTs by total internal reflection.

3.4.1 Main Detector Configurations

The experiment had two different modes of collecting data, referred to as integrating mode and event mode. For each mode the main detector was modified.

During integrating mode, low-gain bases were fitted to the PMTs. Current from the bases was integrated over each helicity window [32]. The asymmetry measurements were made in integrating mode and, in this mode, the bulk of all data were collected.

During event mode, high-gain bases were fitted to the PMTs. Event mode was designed to permit counting of individual pulses in the PMTs, for use in measurements of Q^2 and for background characterizations.

Additionally, the spectra of pulse heights were important tools for discriminating the scattered electrons from a background of pions. The beam current was reduced over six orders of magnitude to currents as low as 50 pA. The trigger during event mode could be set to any of the various detectors, including the main detectors or the

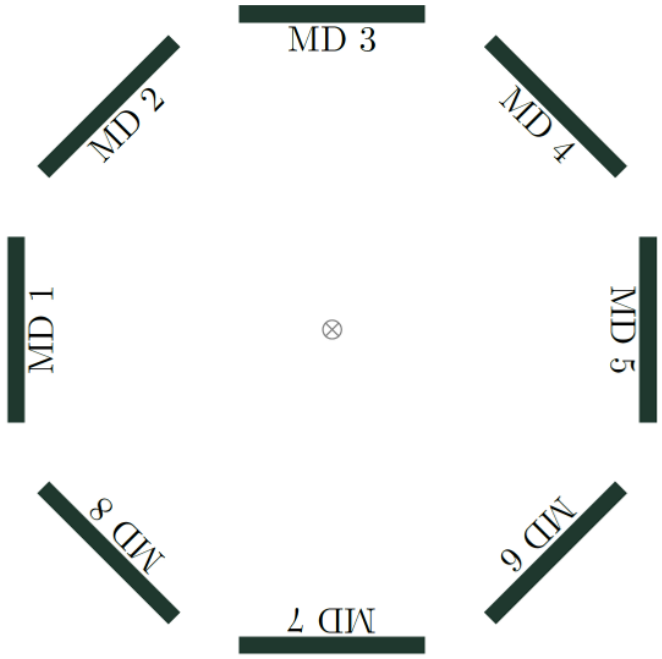

Figure 3.5: Diagram indicating the numbering scheme of the main detectors, when facing downstream. Main detector 7, the lower most detector, had a 4 in thick lead wall installed on its upstream face (see Fig. 3.7).

trigger scintillators.

Since the scattered particles are relativistic charged particles with velocities greater than the local phase velocity of light in that medium, they create a cone of light (Cerenkov Radiation) in the main detectors. For the scattered electrons, this effect was enhanced by 2 cm thick lead pre-radiators which were placed on the upstream face of the detectors. These pre-radiators enhanced the light generated by incoming scattered electrons and also absorbed unwanted low-energy incident particles. Pions, being minimum ionizing particles at the relevant energies [41], do not create additional showers in the pre-radiator. The combined effect caused the pulse height coming from electrons to be about 5 times that coming from pions.

For the present analysis, integrating mode data combines the asymmetry and yield contributions of scattered electrons and pions (there are almost no pions in the 'main' experiment). Event mode data was needed to separate the signal fractions based on the pulse height observed in the PMTs, where scattered electrons typically had a pulse height of $\sim$100 photo-electrons, and pions typically had pulse heights of $\sim$20 photo-electrons. The thickness of the pre-radiators was chosen to maximize the size of the electromagnetic shower and electron signal amplification. Fig. 3.6 shows how the two particle types manifest in the event mode ADC data.

3.4.2 Lead Wall

The measurement described in this thesis has a large background contribution from pions from photo-production. In order to characterize and correct for this, a 10.2 cm thick lead wall was placed in front of the lowest main detector, main detector 7 (MD7) (see Fig. 3.7).

The lead wall attenuates electrons ($\sim$ 18 radiation lengths) passing through with greater effect than on pions. This results in the asymmetry measured in MD7 being dominated by the pion contribution, transforming MD7 into an effective pion detector. MD7 therefore has a different linear combination of electrons and pions contributing to the measured asymmetry than the other seven detectors.

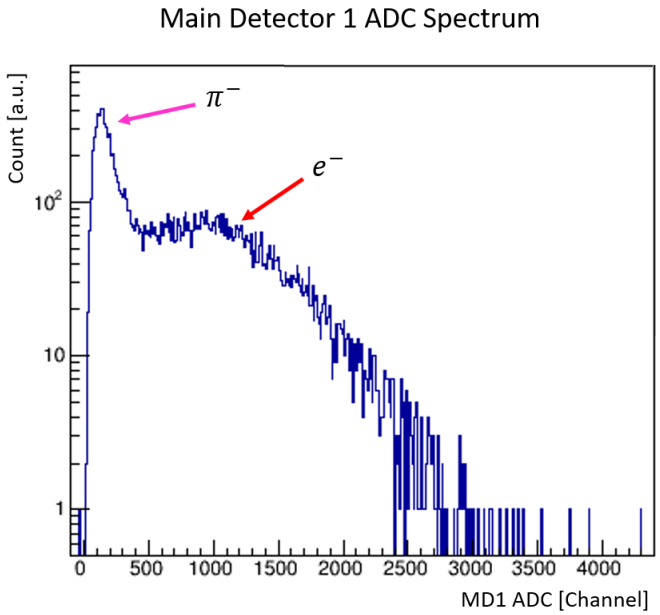

Figure 3.6: Typical pulse-height spectrum obtained from summing a main detector's two PMT ADCs. The magenta arrow indicates the narrow peak due to pions and the red arrow indicates the broad peak due to electrons.

These two distinct linear combinations, in conjunction with a measurement of the pion background fraction, allow the separation of asymmetries arising from scattered electrons and pions (see Sec. 4.2.1 and Sec. 4.2.2).

3.5 Collimation System and Shield-Hut

The acceptance of the experiment was defined by three lead-antimony (95.5% Pb, 4.5% Sb) collimators (see Fig. 3.1). Each collimator contained eight sculpted openings that allowed scattered particles to pass into each of the experiment's octants and restricted the scattering angular acceptance to $5.8^\circ < \theta < 11.6^\circ$ [32]. The first collimator, centered 74 cm downstream of the target, was 15.2 cm thick. A pair of 5 cm thick retractable Tungsten blocks, or 'shutters', were positioned, in opposing octants, on the downstream face of the first collimator. These Tungsten shutters could be inserted so as to block scattered particles in two octants and were used for dedicated background studies. The central aperture of the first collimator, where the beamline passed through, was

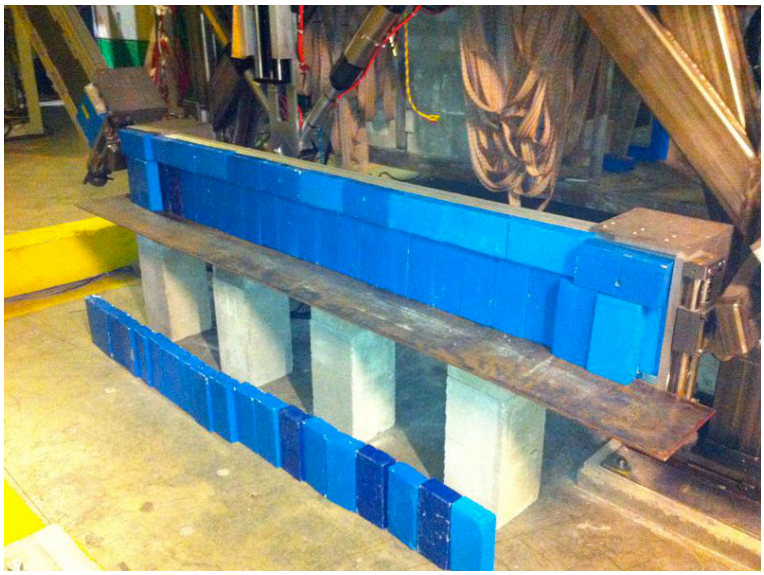

Figure 3.7: A 10.2 cm thick lead wall was installed on the upstream face of main detector 7 to effectively create a pion detector. The wall is constructed from individual lead bricks (blue, middle of photo), each measuring 5.1 cm × 10.2 cm × 20.3 cm. In this picture, one layer of lead bricks (seen on the floor) was removed for a systematic study.

'plugged' by a 21 cm long water-cooled tungsten-copper collimator, called the tungsten plug (Fig 3.8). The tungsten plug was designed to block electrons which scattered at very small angles (∼0.75 to 4.0°), which would have struck the beamline downstream of the first collimator. The second collimator was 15.0 cm thick and centered 2.72 m downstream of the target. The final collimator was placed just upstream of the magnet, 3.82 m from the target center and was 11.2 cm thick.

The main detectors were enclosed in a concrete shielding hut, with 122 cm thick walls. The upstream face was constructed of 80 cm thick high-density (2700 kg/m^3) barite-loaded concrete (Ba_2SO_4). The shield-hut was not designed with 3.35 GeV beam in mind. This became an issue for the present analysis, which is discussed in more detail in Sec. 4.4.1.

Figure 3.8: Picture of the tungsten plug in the central aperture of the collimator closest to the target. Acceptance holes are also visible.

3.6 Tracking System

The Q_{weak} tracking system was employed during the low beam current (50 pA to 200 nA) event mode data collection, in order to extract the acceptance-averaged Q^2 ($\langle Q^2 \rangle$) of the asymmetry measurement. The tracking system included two packages, each consisting of two vertical drift chambers (VDCs), two horizontal drift chambers (HDCs), and one scintillator.

The VDCs and scintillators were mounted downstream of the QTor magnet on a rotation system that allowed two octants on opposite sides of the beampipe to be instrumented simultaneously. Similarly, the HDCs were mounted on a separate rotation system upstream of the QTor magnet.

The tracking chambers could be rotated about the beam axis to cover all four pairs of octants. For redundancy, each rotation system allowed one octant pair to be instrumented with either set of drift chambers.

During integrating mode, the flux of scattered particles was too great for the tracking chambers to handle, so the entire tracking system was retracted out of the experiment's acceptance. A more detailed overview of the tracking system can be found in [32]. See also relevant dissertations which contain in-depth descriptions of each component (HDCs [42], VDCs [43, 44], and scintillators [45, 46]).

3.7 Luminosity Monitors

Two sets of auxiliary detector arrays, called luminosity monitors (lumis), were used during the experiment. These detectors made use of radiation-hard Spectrosil 2000 quartz to withstand the high flux that they were subjected to. Each luminosity monitor was equipped with long light guides to prevent the PMTs from getting large doses of radiation.

Four upstream lumis, each measuring 7 cm × 27 cm × 2 cm, were placed azimuthally, 2.67 m downstream of the target, at a scattering angle of about 5°. The upstream lumis were used to examine correlations between beamline background asymmetries measured with various configurations of other background detectors in the main detector shield-hut (See Sec. 4.4.4).

The four downstream lumis were placed 17 m downstream of the target, at radial positions corresponding to a scattering angle of 0.5°. Each of these lumis measured 4 cm × 3 cm × 1.3 cm with a 45° taper at one edge and utilized a 2 cm thick pre-radiator in front of it to suppress low energy backgrounds.

3.8 Software

The simulation packages used in this experiment were GEANT3, GEANT4, and GARFIELD. GEANT3 was used to simulate the initial experiment and design, and to optimize the geometry of the experiment to attain the desired energy and angular acceptance. GEANT3 was also used in aluminum target cell background simulations.

GEANT4 was used to characterize the main detector photoelectron yield. It was also leveraged for tracking data analysis. Specific event generators for elastic and inelastic ($\vec{e}p$) scattering and pions from photoproduction were also implemented using GEANT4. A generator for highly radiated elastic and inelastic events using the full Mo-Tsai formalism [17] was simulated using GEANT4 as well.

Finally, GARFIELD was used to optimize the design of the HDCs and VDCs, including wire positions, cathode plane spacing, and the gas mixture used.

3.9 Data Acquisition

The experimental apparatus was configured in two distinct data collection modes: integration mode and event mode, see Fig 3.9. The two modes were mostly independent of each other.

Integration mode was used to achieve the high level of statistics necessary for a high precision asymmetry measurement. At beam currents up to 180 µA, data were received so quickly that the photo-electron signal in the main detectors never completely attenuates before the next incident event arrives. The resultant overlapping signals prevents distinguishing individual events. To overcome this complication, the signal is integrated over each helicity window, in order to look at the total light yield and average asymmetries in that given helicity state. The majority of the experiment was conducted in integrating mode and is the source of the primary experimental measurement.

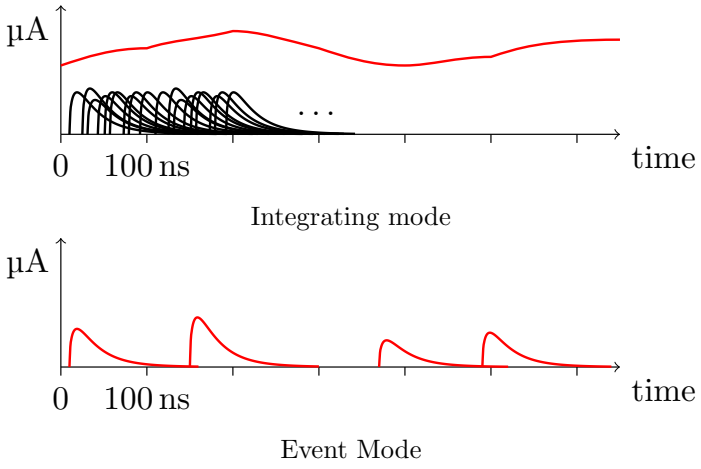

Figure 3.9: Illustration of the difference between integrating mode (top) and event mode (bottom). When the apparatus is configured in integrating mode, individual events cannot be separated from each other and were therefor integrated over a time interval to measure the total effect. In event mode, individual events were measured and recorded.

Due to the nature of integrating mode, an individual event can not be tracked. In order to map the trajectories of individual events, data was also collected in Event mode, a process that records the detector responses to single events. Event mode, in

conjunction with the tracking system (Sec. 3.6), was used to determine the distributions of Q^2, scattered momenta, scattering angles, and light yield at low beam currents (50 pA to 200 nA). Event mode was also used for characterization of various background fractions.

Chapter 4

Data Analysis

The goal of this analysis was the extraction of the parity-violating inelastic asymmetry from electron-proton scattering. The measured production asymmetries contain contributions from many other sources, including the radiative tail from elastic scattering, pions from photo-production, parity-conserving asymmetries from transverse components of the beam polarization, and several other backgrounds.

The overall strategy of the analysis is based on correcting for the 'neutral' background, characterizing the pion background, extracting the longitudinal electron asymmetry, and removal of all other backgrounds, thereby isolating the parity-violating inelastic electron-proton asymmetry.

The 'neutral' background originated from secondary scattering in the collimators and magnet support structure. The background fraction from 'neutral' particles was determined by subtracting 'punch-through' events from the total neutral background measured in the main detector after vetoing charged particles with the trigger scintillators (Sec. 4.3). The 'punch-through' events were the result of elastically scattered electrons penetrating the shield-hut wall, some of which caused an asymmetry in the main detectors (See Sec. 4.4.1).

To characterize the pion background, the pion fractional light yield and the pion asymmetry were measured (Sec. 4.2.1). Extraction of the longitudinal electron asymmetry required knowledge of the polarization angle and the measured asymmetries from

the transverse data set. The measurements of the polarization angles of the electron beam were used to determine the mixture of longitudinal and transverse polarization of the beam incident on the primary target (Sec. 4.1.2). The transverse component of the production data was corrected for using the purely transverse data set, which thereby isolated the asymmetries due to the longitudinal component (Sec. 4.6.2).

The resulting longitudinal electron asymmetry was then corrected for the magnitude of the overall beam polarization (Sec. 4.1.2) and other remaining backgrounds (Sec. 4.4), leaving the parity-violating inelastic asymmetry of interest (see Fig. 4.1).

Figure 4.1: Flowchart illustrating the analysis strategy employed in this dissertation.

4.1 Data Collection Modes

4.1.1 Event Mode vs Integrating Mode

To maximize the counting statistics of this measurement, the apparatus was primarily configured in integrating mode, where the beam current was up to 180 µA. As a result, the light yield from all processes were integrated together, requiring other specialized measurements or simulations to characterize and correct for each background process.

Event mode data were used to separate the effects of electrons from the effects of pions in the integrating mode data. A special configuration of event mode was used to measure the background arising from neutral particles (Sec. 4.3). Event mode data were primarily triggered by a coincidence of the two PMTs in any of the main detectors, with beam currents typically on the order of a few µA. Pre-scale factors were used when collecting this data to scale down the rate of recorded data. This reduced the effect of deadtime in the data acquisition system.

4.1.2 Beam Polarization

During the data collection period for this measurement, a different experimental hall had priority for selecting the beam energy and polarization. This resulted in the beam arriving at the Q_{weak} primary target with mixed polarization in the horizontal plane. In an ideal world, there would have been access to a purely longitudinally-polarized beam to make the PV asymmetry measurement. Such a beam configuration would have maximized the parity-violating asymmetry and eliminated background arising from transversely polarized beam.

The beam polarization for this experiment is described as follows (see Fig. 4.2):

Due to the spin precession in the bending magnets of the accelerator, the polarization angle of the beam, θ_P, that arrived at the hall was $-19.7^\circ \pm 1.9^\circ$ [47], where a positive angle corresponds to an angle measured from the beam axis ($+z$-axis), rotated towards beam right ($+x$-axis). This resulted in a large undesired transverse component ($\sim 33\%$).

The data set, with mixed polarization, will be referred to as 'Production' data, because it contains the physics asymmetry of interest and the bulk of the total data were taken in this configuration.

Several purely transverse runs (i.e. runs with a beam polarization angle of $92.2^\circ \pm 1.9^\circ$ [47]) were performed to characterize and correct for the transverse component in the production data set. This data set will be referred to as 'Transverse' data.

The overall magnitude of the polarization of the electron beam was $(87.0 \pm 0.6)\%$ for both production and transverse data, as measured by the Møller polarimeter in Hall C [48].

4.1.3 Noise Correction and Pedestal Subtraction

For this measurement, the Analog to Digital Converters (ADCs) of the main detector PMTs were configured with long timing gates ($\sim$1 µs) to accommodate some specialized detectors[1]. This lead to additional noise from 60 Hz line phase that broadened the

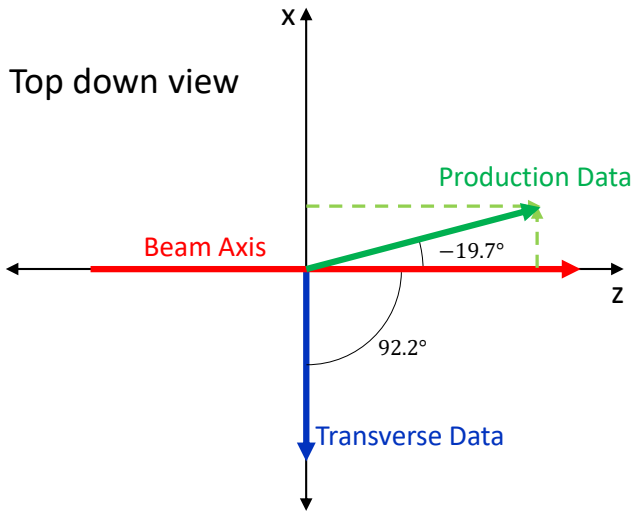

Figure 4.2: Schematic showing a top down view of the polarization angles present during this measurement. The beam axis indicated by a red arrow points in the downstream direction. The 'Production' data (green arrow) had a mixture of longitudinally and transversely polarized electron beam incident on the target. The 'Transverse' data (blue arrow) had, almost exclusively, purely horizontally polarized electron beam incident on the target.

ADC signals, thus reducing the precision of the measurement.

Additionally, during collection of event mode data, the ADCs had an electronic pedestal. An electronic pedestal is defined as the mean value of the signal in the ADC when there are no events in that PMT. The signal from real events in the detector was increased by the value of the pedestal. The pedestal must be measured and subtracted from the ADC value to determine the actual zero of that channel.

The pedestal and any correlated noise between different ADC channels were corrected by examining the correlation between the pedestal of the ADC of interest and a separate 'witness' channel (see Fig. 4.3). The witness channel was another detector channel in the apparatus that was not connected to an actual detector. Since it was not connected to a detector, the witness channel only recorded pedestal. Thus, any noise present in the electronics was evident in the fluctuations or stability of the

[1] Aerogel and Lead Glass detectors were periodically installed, with the intention of using them for pion identification. However, they did not prove to be particularly helpful.

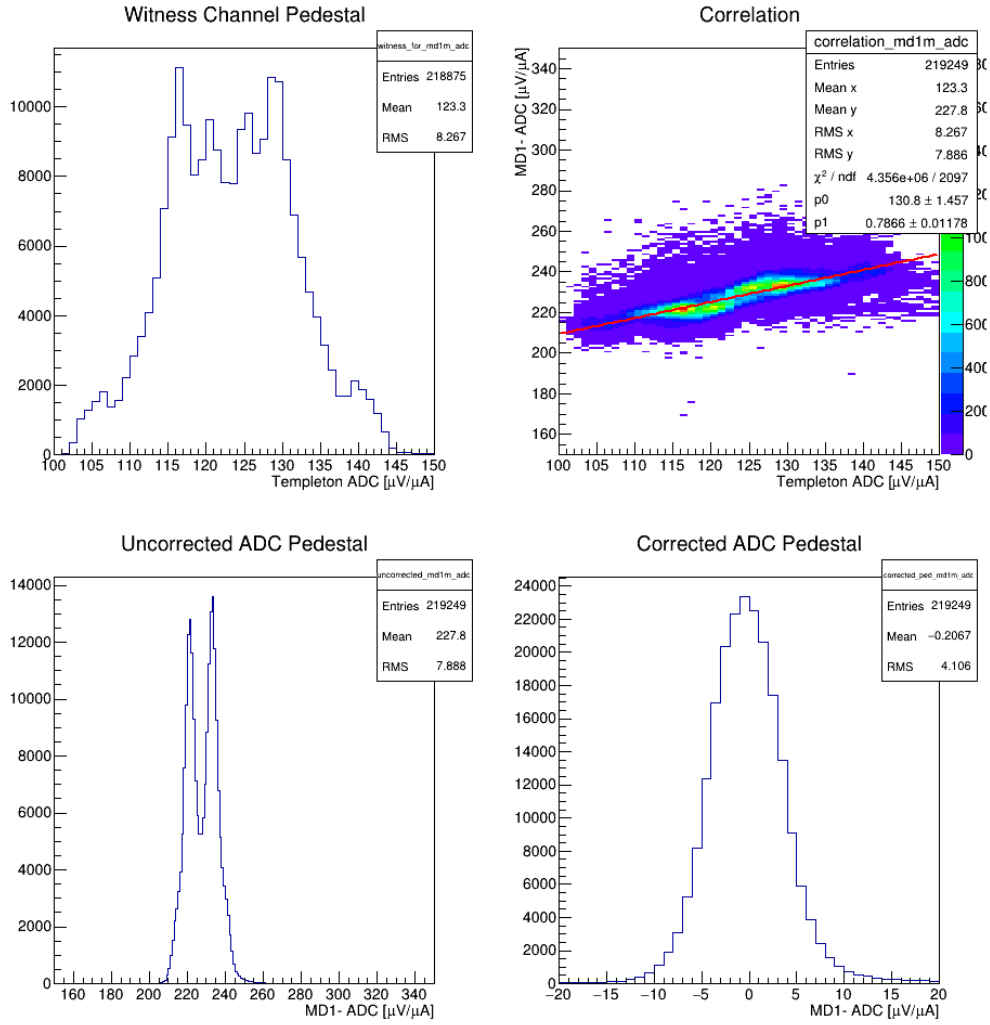

Figure 4.3: (bottom left) The ADC spectrum from a typical main detector PMT (MD1) has a pedestal which shows clear double peaking indicating additional noise. The pedestal of the witness channel ADC (top left) also shows the double peaking. A linear fit (red line) gives the correlation between the main detector ADC pedestal and the witness channel pedestal (top right). After subtraction of the pedestal and correction for the noise (bottom right), the double peaking in the main detector pedestal has disappeared, the root mean squared (RMS) has dropped by almost a factor of two, and the distribution is now centered around zero.

pedestal. It, therefore, was a good measurement of the noise while collecting data.

The correlation slope between the witness channel and the selected main detector channel's pedestal canceled the common-mode noise and zeroed the main detector pedestal. The measured witness channel ADC signal is plotted against the selected

main detector ADC pedestal.

A linear best fit applied to this data yields a correlation slope and intercept (see Fig. 4.3). On an event-by-event basis, the slope and intercept are then applied to the entire main detector ADC spectrum, not just its pedestal. For example, for the MD1-PMT, the following correction was applied to each event in the detectors,

$$X^{MD1-}_{corrected} = X^{MD1-}_{raw} - (p_1 X^{Wit} + p_0), \tag{4.1}$$

where p_1 and p_0 are the slope and intercept, respectively, of the linear fit of the upper right plot in Fig. 4.3, X^{Wit} is the ADC value of the witness channel for that event, X^{MD1-}_{raw} is the raw ADC value of MD1's PMT- for that event, and $X^{MD1-}_{corrected}$ is the ADC value of MD1's PMT- for that event after the corrections have been applied. A similar correction was applied to each PMT of each main detector, thus resulting in cleaner data. Typical pedestal offsets, p_0, were 100 to 200µV/µA and typical correlation slopes, p_1, were 0.6 to 0.8.

4.2 Pion Background

The Q_{weak} apparatus was designed to utilize a 1.16 GeV electron beam and measure elastically scattered electrons, where the scattered energy, E', was very close to that beam energy. In the present ancillary measurement, the beam energy was increased to 3.35 GeV, in an effort to measure inelastically scattered electrons and to put experimental constraints on $\Box_{\gamma Z}$. A side effect of using the apparatus in a configuration where it was not optimized is an unwanted background of pions.

When the incoming 3.35 GeV electrons from the beam interacted with the protons in the ℓH_2 target they could scatter inelastically. This interaction either caused the protons to 'fragment' into many hadrons, with one of the fragments being π's, or caused the protons to enter excited states, such as N^*'s or Δ's. A short time later, the N^*'s and Δ's decayed, mainly into π's and a nucleon[2].

All three types of pions, π^+, π^-, & π^0, were produced. The π^+'s, being positively

charged, had their trajectories bent towards the beam axis resulting in them striking the concrete shield-hut surrounding the main detectors. The π^0's had very short lifetimes ($\sim 10^{-16}$s) and decayed primarily into two photons while still in the target. Since there was no direct line of sight from the primary target to the main detectors, the photons from the π^0's were obstructed from directly hitting the main detectors. The π^-'s have the same electric charge as the electrons and so they were bent in the same outward radial direction by QTor.

As a result, these π^-'s could fall into the acceptance of the experiment. For that to occur, they either had to be emitted within the right energy range, or they had to have radiated enough energy after being emitted to fall into the right energy range.

From here on, 'pions' refers exclusively to π^-'s.

4.2.1 Pion Yield Fraction

When the experiment is configured in integrating mode, the light deposited in the main detectors by the pions is indistinguishable from the light deposited by scattered electrons. This dilutes the signal arising from electrons. The relative light yield from the two particle types was determined based on event mode data.

When the apparatus is in event mode, the light yield, or photo-electron count, of each event that triggers the detector system is recorded, thus yielding distinct, but overlapping photo-electron spectra for each particle type. Electrons and pions, on average, deposit different amounts of photons in the main detectors, resulting in two distinct peaks in the ADC response spectrum of the main detector PMTs (see Fig. 4.4).

Pions at these energies are minimum ionizing particles and, therefore, did not cause significant amounts of showering when passing through the lead pre-radiators and therefore caused only a small energy deposit in the quartz detectors. On average, each pion deposited approximately 20 photo-electrons in the detector.

Electrons, being much less massive, are more likely to be attenuated by the lead of the pre-radiators. As the electron interacts with the lead, energy is lost in the form of emitted gamma rays and each gamma can convert into electron-positron

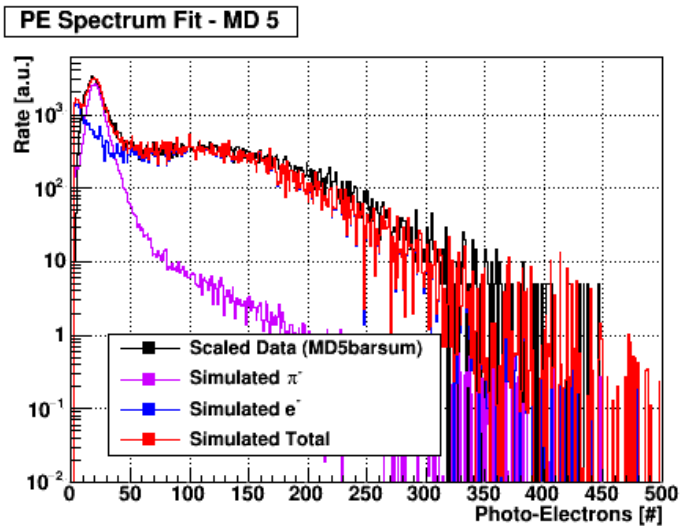

Figure 4.4: Example photo-electron spectrum fit. Two distinct peaks can be seen in the data (black curve). The narrow peak on the left, centered near 20 photo-electrons, is due to pions (simulation: magenta curve). The much broader peak on the right centered near 100 photo-electrons is due to electrons (simulation: blue curve). The red curve is the combined total of the pion and electron simulations.

pairs. With sufficient energy, these secondary electrons or positrons can go on to emit additional photons, amplifying the total number of electron-positron pairs. In this way, incident electrons produce electromagnetic showers in the pre-radiators, yielding copious amounts of electrons and positrons. The resulting shower amplifies the signal of the original electron. The electrons and positrons that are not completely absorbed by the lead, become incident on the main detector and deposit light through Cherenkov radiation. Each incident electron event deposited an average of 100 photo-electrons.

Separate GEANT4 simulations for incident electrons and pions were used to obtain their expected photo-electron distributions. These simulations were compared to pedestal-subtracted data through a MINUIT minimization [49] to determine the relative abundance of electrons and pions. MINUIT is a numerical minimization computer program, widely used in particle physics, that minimizes a user-defined function with respect to multiple parameters.

The overall scaling factors, or normalizations, of the simulated electron and pion photo-electron distributions were allowed to scale independently. This allowed the

fit to be insensitive to incorrectly simulated cross sections, such as due to imperfect knowledge of which process generated the particle, be it scattering from hydrogen or scattering from the aluminum windows; i.e., only the shape of the spectrum was used. This was especially important in the case of the pions, due to limitations on the models for pion production [50] at these kinematics.

The gain of the data, a scaling factor applied to the incoming raw signal, was scaled to effectively convert the ADC channels of the PMTs to the photo-electrons used in the simulations. Scaling in this way preserved the relative mean pulse-heights between the electron and pion simulations. The scaled simulations were then integrated to determine the simulated total light yield for each particle type.

These total light yields were combined to form the pion yield fraction, f_π^i, which is the fraction of the total light yield measured in main detector i (see Fig. 3.5) that come from incident pions.

The pion yield fraction was calculated as

$$f_\pi^i = \frac{Y_\pi^{sim}}{Y_\pi^{sim} + Y_e^{sim}}, \tag{4.2}$$

where i is the detector number, Y_π^{sim} is the total simulated light yield from pions, and Y_e^{sim} is the total simulated light yield from electrons.

In Figure 4.5, the pion fractions for six of the eight main detectors are shown along with the corresponding uncertainties due to the MINUIT minimization. Main detector 3 was not included in this analysis, due to a light leak in one of the PMTs that was discovered after data had been collected[2]. Main detector 7 was not included, because it required a different approach to determine its pion yield fraction (see Sec. 4.2.2).

There was a significantly larger variance in the pion fraction values than what one would expect from statistical uncertainty alone. It was assumed that there was an unaccounted for systematic effect, possibly from some threshold effect. A typical electron deposits $\sim$ 100 photo-electrons (with $\sim$ 50 photo-electrons in each of a

[2]Main detector 3 was still included in the asymmetry analysis, because the light leak was negligible in comparison to orders of magnitude greater event rate in the detector during integrating mode.

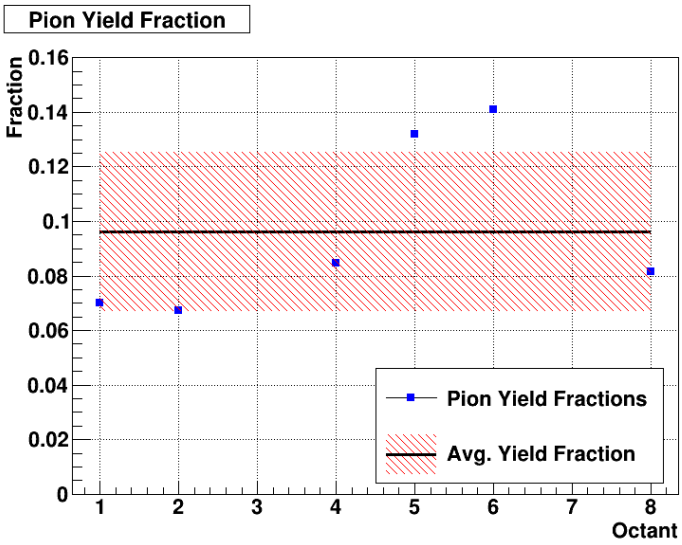

Figure 4.5: Fraction of detector yield due to pions is shown for each main detector, except MD3 and MD7. MD3 was excluded due to a light leak discovered in one of the PMTs. MD7 was excluded because of the presence of the lead wall. The uncertainties for each point are from the uncertainty in the fit routine. Also shown is the mean value (black line) and 1σ RMSD bound on the average (hatched area).

detector's two PMTs), where a typical pion deposits only ~ 20 photo-electrons in total (see Fig. 4.4). Given this disparity in photo-electron yield, adjusting the threshold to cut off one or two photon events will have a much greater effect on the pion signal than on the electron signal. Events that deposit only a few photo-electrons in a PMT are more likely to have originated from a pion event, rather than an electron event, due to the larger number of photo-electrons produced by electrons.

As such, a change in threshold that cuts off low photo-electron events will have a greater effect on the pion detection efficiency than on the electron detection efficiency. This will cause a corresponding change in the measured pion yield fraction that can vary from detector to detector. The pion yield fraction is therefore rather sensitive to where the threshold was set, and is likely the cause of the large variance of the data.

The root mean squared deviation (RMSD) of the six pion yield fractions was used as a conservative uncertainty on the average pion yield fraction to account for this systematic effect, giving and octant-averaged value of $f_\pi^{avg} = 0.096 \pm 0.029$.

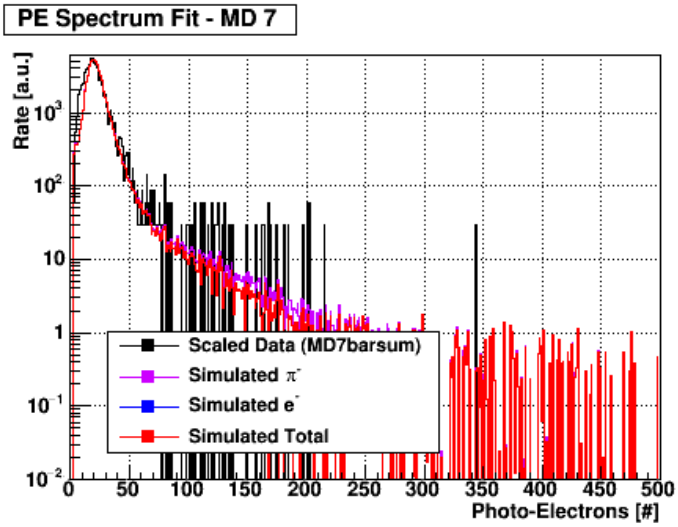

Figure 4.6: Example photo-electron spectrum for MD7. The data (black curve) only shows a single, narrow peak from pions. The peak from the electrons is hidden in the tail of the pion distribution.

4.2.2 Pion Yield Fraction with Pb Wall

The lead wall immediately upstream of MD7 attenuates the electrons incident on the detector (the lead was approximately 18 radiation lengths thick). The more massive incident pions are less affected, which results in a very different photo-electron spectrum than from the other detectors.

It was impossible to separate the light spectra in MD7 using the method described in Sec. 4.2.1, because the electron peak was smaller than the statistical fluctuations in the tail of the pion distribution (see Fig. 4.6). There were not enough statistics to reliably fit both the simulated pion and electron spectra to the data. An alternative method was required to calculate the pion yield fraction in MD7.

The average pion yield fraction for the six other main detectors was converted into a pion-to-electron ratio, $R^{avg}_{\pi/e}$, using

$$R^{avg}_{\pi/e} = \frac{f^{avg}_{\pi}}{1 - f^{avg}_{\pi}} = 0.092 \pm 0.027. \tag{4.3}$$

High statistics GEANT4 simulations of MD7 were used to create signal attenuation

fractions, $\xi_{\pi(e)}$, which indicate the fractional size of pion (electron) signal after passage through the lead wall. They were calculated using

$$\xi_\pi = \frac{Y_\pi^{Pb}}{Y_\pi^0} = 0.608 \pm 0.026 \tag{4.4}$$

and

$$\xi_e = \frac{Y_e^{Pb}}{Y_e^0} = 0.014 \pm 0.002, \tag{4.5}$$

where $Y_{\pi(e)}^{Pb}$ is the simulated yield from pions (electrons) seen in the main detector with the lead wall in place and $Y_{\pi(e)}^0$ is the simulated yield from pions (electrons) seen in the main detector without the lead wall. The signal attenuation fractions were then used to scale $R_{\pi/e}^{avg}$ to calculate the pion-to-electron yield ratio in MD7,

$$R_{\pi/e}^7 = R_{\pi/e}^i \times \left[\frac{\xi_\pi}{\xi_e}\right] = 4.06 \pm 1.35. \tag{4.6}$$

The inverse of Eqn. 4.3 converts $R_{\pi/e}^7$ into a fractional pion yield for MD7,

$$f_\pi^7 = \frac{R_{\pi/e}^7}{1 + R_{\pi/e}^7}. \tag{4.7}$$

The resulting pion yield fraction for MD7 was $f_\pi^7 = 0.81 \pm 0.05$.

4.3 Neutral Background

A soft neutral background arose from secondary scattering of the primary scattered electrons or pions that resulted in a signal in the MDs. Photons and small amounts of neutrons were generated by those primary particles scraping the apertures of the collimators or the shield wall edges.

The effect of this neutral background was measured in event mode using the trigger scintillator to veto charged particles. It was assumed that any event that triggered the MD, but failed to trigger the trigger scintillator was a neutral particle. This assumes that all particles that trigger the MDs have trajectories that pass through the trigger

scintillators. Using this method, the fractional light yield in the MDs that originated from these neutral particles was measured to be [51]

$$f_{veto} = 0.078. \tag{4.8}$$

This yield fraction is only valid for the seven unblocked MDs, because MD7 detected a much smaller rate of non-neutral events. Thus, the signal in MD7 was more greatly diluted by these neutral particles.

Because the lead wall extended upstream from MD7, the trigger scintillator could not be positioned to make a similar neutral background measurement for MD7. They could only be used to make this measurement in MD1 and MD5. It was assumed that these measurements were correct for all seven unblocked MDs, due to the symmetry of detector placement. Other available data and extensive simulations were required to calculate an estimate of the effect of neutral particles in MD7.

One can imagine charged particles that undergo multiple scattering and strike the MD at steep angles, thus bypassing the trigger scintillators. These events would then be included in f_{veto}, but were not necessarily neutral particles. The punch-through events discussed in Sec. 4.4.1 were one such source of events that bypassed the trigger scintillators (see Fig. 4.7).

4.3.1 Yield Ratio from Data

The neutral background in MD7 was calculated using several different simulations. The ratio of yields measured from data was used as a benchmark to gauge the accuracy of that calculation. That ratio was

$$\frac{Y_7^{data}}{Y_{UB}^{data}} = 13.9\%, \tag{4.9}$$

where Y_7^{data} is the average yield measured in MD7's two PMTs and Y_{UB}^{data} is the average yield measured in the 14 PMTs of the seven unblocked MDs. This ratio from data was

compared to a similar ratio calculated using GEANT4 simulations, as described below.

This ratio was recreated using simulation, because the level of agreement between the data and the simulation was an indication of how well the neutral background was understood.

4.3.2 Calculated Yield for Unblocked Main Detectors

To re-create the yield ratio in Eqn. 4.9 using simulation, the simulated yields in the unblocked MDs and MD7 must both be determined.

In the GEANT4 simulations, there were two different event types used to simulate scattered electrons. The first, called event type 1, or ET1, was designed primarily to simulate elastic scattering of electrons near the elastic peak. ET1 was used when calculating the punch-through events (Sec. 4.4.1). The second event type used was called event type 7, or ET7. ET7 was designed to simulate highly radiated elastic and inelastic scattering.

The simulated light spectrum from scattered electrons used in the pion yield fraction analysis (Sec. 4.2.1) contains contributions from highly radiated elastic and inelastic scattering, as well as punch-through events. The simulated rates from the various processes were used to calculate the fractional rate that originated from events that were *not* punch-through events, β_e, as follows:

$$\beta_e = \frac{R_{ET7}}{R_{ET7} + R_{ET1}^{PT}} = 0.923. \tag{4.10}$$

R_{ET1}^{PT} is the simulated rate of scattered electrons that resulted in punch-through events. R_{ET7} is the combined simulated rates of highly radiated elastic and inelastic scattering. The punch-through events were treated separately in another analysis, so their effect must be removed here.

The simulated fits to data seen in Fig. 4.4, for both electron and pion events, were integrated separately. This resulted in calculations of the total event rate of scattered electrons, R_e, and pions, R_π. Applying β_e to R_e gives the total rate of scattered

electrons from all other processes excluding punch-through events,

$$R'_e = \beta_e R_e, \tag{4.11}$$

where R'_e was the modified total rate of scattered electrons. These rates were used to form rate fractions:

$$F_\pi = \frac{R_\pi}{R_\pi + R'_e} = 0.269$$

$$F_e = \frac{R'_e}{R_\pi + R'_e} = 0.731 \tag{4.12}$$

These rate fractions indicate the relative flux of electrons versus pions incident on the main detectors. The average number of photo-electrons deposited in the unblocked MDs was simulated to be

$$\gamma_\pi^{UB} = 22.5\,\text{PEs} \tag{4.13}$$

for pions and

$$\gamma_e^{UB} = 98.3\,\text{PEs} \tag{4.14}$$

for scattered electrons. A rate times the average number of photo-electrons gives the total light yield for that process. Combining the simulation rates and average photo-electron counts for electrons and pions gives the average expected light yield for the unblocked MDs as

$$\gamma_{UB} = F_\pi \gamma_\pi^{UB} + F_e \gamma_e^{UB} = 77.9\,\text{PEs}. \tag{4.15}$$

4.3.3 Calculated Yield for MD7

To calculate a similar relative light yield for MD7, additional information must be known. It is necessary to know the survival rate of electrons and pions traversing the lead wall, as well as, how the average number of photo-electrons deposited has changed due to the presence of the lead wall.

The event rate for electrons and pions must be simulated, both with and without

the lead wall, to calculate the survival fraction in terms of rate. In a similar manner as the survival yield fractions (Eqn. 4.4), the survival rate fractions are formed by forming the ratios,

$$S_\pi = \frac{R_\pi^{Pb}}{R_\pi^0} = 0.668 \tag{4.16}$$

and

$$S_e = \frac{R_e^{Pb}}{R_e^0} = 0.160. \tag{4.17}$$

$R_{\pi(e)}^{Pb}$ is the simulated rate of pions (electrons) seen in the main detector with the lead wall in place and $R_{\pi(e)}^0$ is the simulated rate of pions (electrons) seen in the main detector without the lead wall.

The average number of photo-electrons deposited in the MD with the wall was simulated to be

$$\gamma_\pi^7 = 20.5 PEs \tag{4.18}$$

for pions and

$$\gamma_e^7 = 8.4 PEs \tag{4.19}$$

for electrons. Note that the average number of photo-electrons produced by scattered electrons has been significantly reduced compared to the simulation without the lead wall. The photo-electron count from pions is much less affected.

Now, to calculate the expected yield in MD7, the relative rate fractions in Eqn. 4.12, F_π and F_e, are attenuated by the survival fractions S_π and S_e, resulting in

$$\gamma_7 = S_\pi F_\pi \gamma_\pi^7 + S_e F_e \gamma_e^7 = 4.67\,\text{PEs}. \tag{4.20}$$

4.3.4 Calculating the Neutral Background Fraction

The two calculated expected light yields, γ_{UB} and γ_7, are missing the effect of neutral particles. There was not a direct way to simulate the neutral background. The neutral yield fraction was, instead, calculated from a combination of data and simulations of all other processes. The combined effect of the punch-through events and neutrals in

the unblocked MDs was measured from data in Eqn. 4.8, using the trigger scintillator as a veto. Broken down into the two contributions, f_{veto}, can be written as

$$f_{veto} = f_{NB} + f_{PT}, \tag{4.21}$$

where f_{NB} is the fractional light yield originating from neutral events, and f_{PT} is the fractional light yield from punch-through events. All fractional light yields are defined as

$$f_{\epsilon} = \frac{Y_{\epsilon}}{Y_{Tot}^{sim}} \tag{4.22}$$

for $\epsilon = [\pi, e, PT, NB, veto]$, where Y_{ϵ} was the yield from process ϵ and $Y_{Tot}^{sim} = Y_{\pi} + Y_{e} + Y_{PT} + Y_{NB}$. By extension of the previous two equations,

$$Y_{veto} = Y_{NB} + Y_{PT}. \tag{4.23}$$

From simulation, the yield from pions in the unblocked MDs was

$$Y_{\pi} = 1420\,\mathrm{PE}\cdot\mathrm{kHz}/\mu\mathrm{A}. \tag{4.24}$$

For punch-through events, the yield was simulated to be

$$Y_{PT} = 76.5\,\mathrm{PE}\cdot\mathrm{kHz}/\mu\mathrm{A}. \tag{4.25}$$

For non-punch-through scattered electrons, the yield was

$$Y_{e} = 3369\,\mathrm{PE}\cdot\mathrm{kHz}/\mu\mathrm{A} \tag{4.26}$$

Invoking unitarity, the sum of the yield fractions for all processes must equal unity, therefore

$$1 = f_{\pi} + f_{e} + f_{PT} + f_{NB} = f_{\pi} + f_{e} + f_{veto}. \tag{4.27}$$

Each yield fraction is dependent on Y_{Tot}^{sim}. Of the individual yield contributions to

Y_{Tot}, only Y_{NB} was unknown. Eqn. 4.27 was combined with the definition of Y_{Tot}^{sim} to form

$$1 - f_{veto} = \frac{Y_\pi + Y_e}{Y_{Tot}^{sim}}. \tag{4.28}$$

Through some algebra, this equation can be rearranged to solve for Y_{NB}, leaving only known quantities on the right side of the equation,

$$Y_{NB} = \frac{(Y_\pi + Y_e) f_{veto}}{1 - f_{veto}} - Y_{PT} = 328.6\,\mathrm{PE} \cdot \mathrm{kHz}/\mu\mathrm{A}. \tag{4.29}$$

With Y_{NB} known, the fractional light yield from neutral particles in the unblocked MDs was calculated to be

$$f_{NB} = \frac{Y_{NB}}{Y_{Tot}^{sim}} = 0.063 \pm 0.006 \tag{4.30}$$

A conservative 10% relative uncertainty was applied to this calculation to account for assumptions made along the way.

4.3.5 Accounting for Neutral Particles

The neutral background fraction was then used to modify the relative light yield for the unblocked MDs (Eqn. 4.15), giving

$$\gamma'_{UB} = \gamma_{UB}(1 + f_{NB}) = 82.8\,\mathrm{PEs}. \tag{4.31}$$

Therefor, the relative light yield from neutral particles was

$$\gamma_{NB} = \gamma_{UB} f_{NB} = 4.9\,\mathrm{PEs}. \tag{4.32}$$

Recall that all neutral events are defined as events that do not trigger the trigger scintillator. The lead wall and the trigger scintillator were both located just upstream of the MDs, and both covered approximately the same solid angle with respect to the MDs. Any neutral or charged particle that would bypass the trigger scintillator, would

also most likely bypass the lead wall. Thus, MD7 should experience the same absolute rate and yield from neutral particles as the unblocked MDs. As above, the neutral background modified the expected light yield for MD7 as,

$$\gamma_7' = \gamma_7 + \gamma_{NB} = 9.6\,\text{PEs} \tag{4.33}$$

The fractional light yield in MD7 from the neutral background can then be calculated from simulation as

$$f_{NB}^7 = \frac{\gamma_{NB}}{\gamma_7'} = 0.514 = 51.4\%. \tag{4.34}$$

The modified relative light yields, Y_{UB}' and Y_7', were then used to form the ratio

$$\frac{\gamma_7'}{\gamma_{UB}'} = \frac{9.6\,\text{PEs}}{82.8\,\text{PEs}} = 0.116 = 11.6\% \tag{4.35}$$

Recall that the same ratio calculated from data (Eqn. 4.9) was 13.9%. The relative difference between simulation and data was 16.8%. This deviation was used as a reasonable conservative uncertainty on the determination of the neutral background fraction in MD7. Thus, the final neutral background fractions and their uncertainties were

$$f_{NB} = 0.063 \pm 0.006 \tag{4.36}$$

and

$$f_{NB}^7 = 0.51 \pm 0.09. \tag{4.37}$$

4.4 Additional Backgrounds

The primary mode of data collection was in integrating mode, where signals from all sources in a particular detector PMT are integrated together. This means that undesired events cannot be rejected beforehand through pre-event selection. Instead, they must either be suppressed through design or corrected for after the fact. Their contributions need to be characterized either through simulations or through dedicated

studies. Several unwanted backgrounds were present in this measurement that diluted the signal of interest. In general, each background has two important attributes: a background yield fraction and an associated asymmetry.

A yield is defined as the product of the event rate and the photo-electron response in the detectors, normalized to the beam current. A background yield fraction is thus the fraction of the total detected yield that originates from a specific source and is defined as

$$f_i = \frac{Y_i}{Y_{Tot}} \tag{4.38}$$

where $i = [El, PT, Al]$. The total light yield, Y_{Tot}, is given by,

$$Y_{Tot} = Y_{Inel} + Y_{El} + Y_{PT} + Y_{Al}, \tag{4.39}$$

where Y_{Inel} is the simulated light yield of inelastically scattered electrons, Y_{PT} is the simulated light yield from punch-through events, and Y_{Al} is the simulated light yield of electrons scattering off of the Al target windows.

Each of these backgrounds are detailed below.

4.4.1 Shield-Hut Punch Through

The shield-hut enclosed the main detectors and other parts of the apparatus (see Sec. 3.5 and Fig. 3.1). It was designed to shield the main detectors from backgrounds resulting from the experiment's intended 1.16 GeV electron beam. In conjunction with QTor's magnetic field, ∼1.16 GeV elastically scattered electrons were steered through the apertures of the shield-hut and focused on the main detector bars. Any less energetic electrons were swept more radially away from the beam axis, preventing transit through the shield-hut apertures.

For this measurement, the beam energy was 3.35 GeV. Elastically scattered electrons preferentially scatter with very little energy loss. Therefore, the scattered energy distribution is highly 'peaked' near the beam energy. This means that the majority of the elastically scattered electrons retained an energy very close to 3.35 GeV.

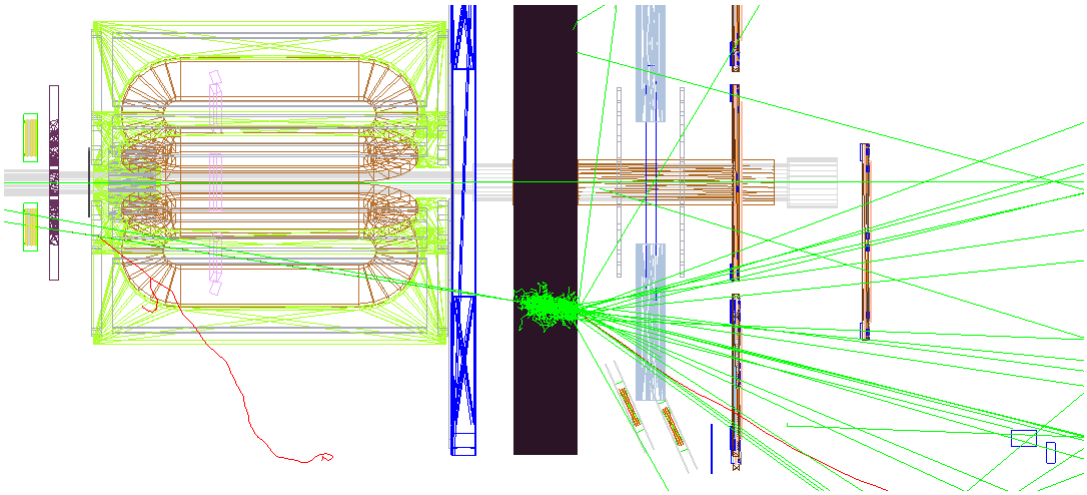

Figure 4.7: Sample simulated event illustrating the shield-hut punch through. A side view of the simulated apparatus is shown. The rings on the left are the magnetic coils of QTor, the vertical black bar in the center is the shield-hut wall, and the orange and blue bars on the right are the main detectors. The target is to the left, outside the field of view of this picture. The green lines represent the trajectories of photons, and the red lines represent electrons. Coming in from the left is a scattered electron and a photon travelling parallel to each other (the red line of the electron is obscured by the photon). They strike the shield-hut wall and create a shower, which is partially absorbed. Some portion of the shower punches through to the other side of the wall and strikes the main detectors. Note that the trigger scintillator (vertical blue line just upstream of the lowest MD) was completely bypassed by this event.

QTor was tuned to select ∼1.16 GeV electrons, so the higher energy electrons in the elastic peak were not sufficiently deflected to pass through the apertures of the shield-hut. This resulted in all of the elastic peak electrons (~ 3.35 GeV), which made it through the collimators, slamming directly into the shield-hut wall, between the apertures and the beam axis.

These electrons created showers of particles as they traversed the concrete wall. Some fraction of these showers were absorbed completely by the wall. For others, a part of the resulting shower managed to penetrate or *punch through* the wall, scatter inside the shield-hut, and ultimately deposit light in one or more of the main detectors. This unwanted background had its own associated asymmetry, which diluted the inelastic asymmetry measurement of interest.

To correct for this, GEANT4 was used to simulate elastically scattered electrons with

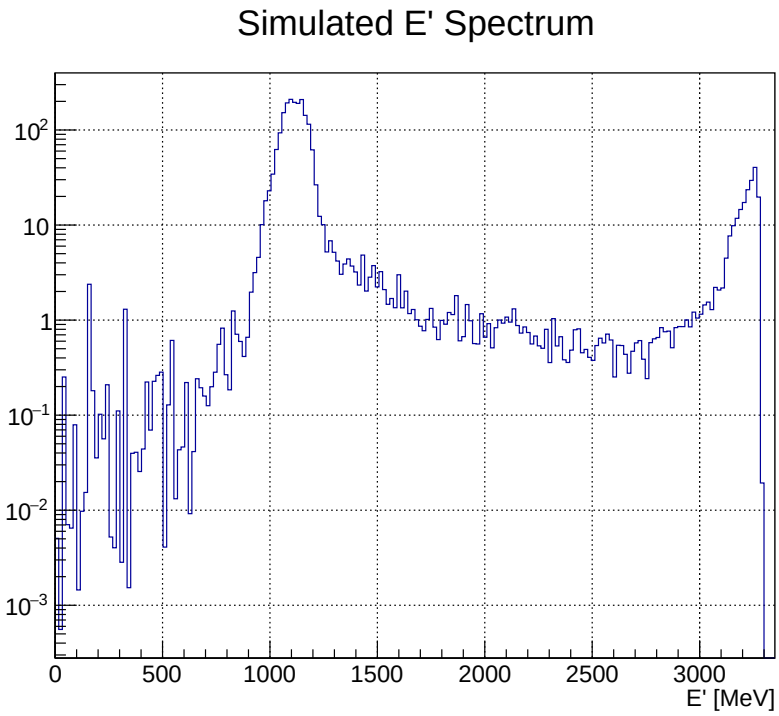

Figure 4.8: This plot shows the energy spectrum of elastically scattered electrons that trigger the main detectors. These data were generated using the GEANT4 simulation of the Q_{weak} apparatus. The vertical axis has arbitrary units, which indicate a logarithmic scale of relative frequency, weighted by cross section and photo-electron yield. Note the two distinct peaks. The left most peak, at roughly 1100 MeV, is composed primarily of highly radiated scattered electrons that pass through the collimators and the apertures of the concrete shield-hut, to directly impinge on the main detector. The right most peak is primarily composed of elastically scattered electrons which had radiated very little energy. These electrons traversed the collimators, but struck the shield-hut wall, creating a shower that triggered the main detector (see Fig. 4.7).

scattered energies ranging from 150 MeV up to 3.35 GeV (Fig. 4.8 shows the spectrum of scattered energies of those electrons that deposit light in the main detector).

There were two distinct and highly separated peaks in this spectrum. Those events in the left peak, centered close to 1 GeV, are the highly radiated elastically scattered electrons. They radiated enough energy that the magnetic field of QTor could steer them through the apertures of the shield-hut. These events were previously discussed in Sec. 4.4.2.

The events in the right peak, near the beam energy, are elastically scattered

electrons that radiated little to no energy. These are the events that slammed into the shield-hut, created a shower of secondary particles that was partially absorbed, and still triggered a main detector. These are referred to as the punch-through events.

In terms of event rate seen in the main detectors, the latter process occurred about a third of the time with a fractional probability of 0.34 compared to the total rate of elastically scattered electrons. From GEANT4 simulations, the asymmetry of these punch-through electrons was found to be

$$A_{PT} = -3.96 \pm 0.04\,\text{ppm}. \tag{4.40}$$

4.4.2 Elastic Radiative Tail

For the weak charge measurement, elastically scattered electrons were the signal of interest and inelastically scattered electrons were an unwanted background. However in the ancillary measurement presented here, the reverse was true. Elastically scattered electrons were an unwanted background, diluting the signal of interest, the *inelastically* scattered electrons. The energy spectrum of elastically scattered electrons is highly peaked near the incident energy (Sec. 4.4.1 details the effect of electrons in the peak). This spectrum has a long tail, with decreasing probability as the scattered energy decreases.

To make it into the momentum acceptance of the apparatus and thus contribute to the background, the electron must shed approximately 2.2 GeV. The most probable process that allows this is the radiation of a single high-energy, or 'hard', bremsstrahlung photon [52]. This can occur either before the scattering interaction on the incident electron, or after the scattering interaction on the scattered electron.

It is also possible for two or more bremsstrahlung photons to be emitted by the electron. However, this is much less likely, because each bremsstrahlung photon radiated reduces the cross section, or probability, of that interaction occurring by roughly a factor of the fine structure constant, $\alpha \approx 1/137$.

For this measurement, the asymmetry was determined through the use of a GEANT4

simulation. Elastically scattered electrons were generated and propagated through the simulated apparatus. Each scattering event was weighted by the Mott cross section with a correction for recoil of the target proton. Additionally, each event is weighted by their light-yield in the main detectors. The Born cross sections were modified by the "Schwinger Correction" to account for the effects of 'internal' radiation [53]. Corrections for 'external' radiation were performed by the GEANT4 physics engine. The scattered energy distribution of these simulated events is shown in Fig. 4.8. Those events with scattering energy, $E' \leq 1.55\,\mathrm{GeV}$, contribute to the asymmetry of the elastic radiative tail. Those with scattering energy, $E' > 1.55\,\mathrm{GeV}$, contribute to the asymmetry of the 'punch-through' events described in Sec. 4.4.1. The 1.55 GeV threshold was chosen because it was the upper range limit of the physics event generator in the GEANT4 simulation that was designed to simulate highly radiated events. The exact position of the threshold on E' has a negligible effect, because it lies in a region where the E' acceptance is suppressed by at least an order of magnitude (see Fig. 4.8).

The asymmetry of the elastic radiative tail, as determined from simulation, is $A_{El} = -0.58 \pm 0.02\,\mathrm{ppm}$.

Knowledge of the relative cross sections of both radiated elastic and inelastic scattering is essential for the determination of the light yield fraction arising from the radiated elastic electrons. The cross sections and their radiative corrections have been thoroughly examined in Mo and Tsai [17], and further refined in Tsai [52] and Christy and Bosted [54].

The calculations of the necessary radiative corrections to the cross section were too computationally expensive to directly embed in the simulation. Instead, the cross sections were calculated using an external piece of computer code originally written by S. Dasu [55], which was modified by several other people. In it, the Mo and Tsai elastic, inelastic, and quasi-elastic cross section calculations were implemented (detailed in Appendix C of Ref. [55]).

Additional approximations and corrections were necessary. The angle-peaking approximation was used when calculating the angular integration of the cross sections.

This approximation is the assumption that if photons are emitted, their momentum will preferentially be parallel to the electron's momentum.

Additionally, the equivalent-radiator approximation was used to calculate the internal Bremsstrahlung corrections. The effect of the internal Bremsstrahlung on inelastic scattering is equivalent to placing one radiator before the scattering and another radiator of the same thickness after the scattering.

In Mo and Tsai [17], these two approximations were compared to the exact formulas and found to work very well in the kinematic regime of this experiment (agreement at the $\sim 5\%$ level).

An additional Coulomb-correction [56] was included, which corrects for the acceleration or deceleration of the electron when it encounters the Coulomb field of the nucleus from which is scatters. Essentially, the Coulomb field induces a small change in kinematics in the reaction.

These calculations were necessary to calculate the proper relative cross sections of elastic versus inelastic scattering. The cross sections were used to weight the simulated events and used to calculate the light yield fraction of elastic scattering, f_{El}, as follows:

$$f_{El} = \frac{Y_{El}}{Y_{Tot}} = 0.62 \pm 0.04, \tag{4.41}$$

where Y_{EL} is the simulated light yield of the radiative tail of elastically scattered electrons.

4.4.3 Al Target Windows

Another background arose from electrons scattering off the windows of the aluminum vessel containing the primary liquid hydrogen (ℓH_2) target. Incoming electrons in the electron beam had to pass through the upstream face, or 'window', of the aluminum target vessel to reach the ℓH_2 in the target. After unscattered electrons in the beam passed through the ℓH_2, they passed through the downstream face, or 'window', of the aluminum target vessel. Electrons could scatter off either of these aluminum windows.

If electrons scattered from the Al windows with the right energy and angle, they would make it into the acceptance of the apparatus and hit one of the main detectors. The light deposited in the main detectors from these events and their contribution to the measured asymmetries were an unavoidable background.

The aluminum window background had two components: the fractional light yield in the detectors from electrons that scattered off of the aluminum windows and the asymmetry that they carry. To determine the fractional light yield contribution from the aluminum target windows, f_{Al}, GEANT4 simulations were employed.

In the simulation, electrons were scattered specifically off the aluminum windows and the total light yield, Y_{Al}, weighted by cross section, was calculated. The total light yield from the aluminum was divided by the combined total simulated light yields from all processes involved (Eqn. 4.39), forming the background fraction,

$$f_{Al} = \frac{Y_{Al}}{Y_{Tot}} = 0.0075 \pm 0.0009, \tag{4.42}$$

The asymmetry from the aluminum was measured from dedicated runs, in which the ℓH_2 was replaced with a thick, aluminum dummy target. The dummy target was made of the same aluminum alloy as the vessel containing the ℓH_2 primary target. This measurement necessitated reducing the beam current to 60 µA to avoid depositing too much energy, because the dummy targets did not have ℓH_2 cooling them. The octant dependence of the asymmetry from the aluminum dummy target is shown in Fig. 4.9. The average measured asymmetry from the seven unblocked octants was -3.1 ± 2.2 ppm.

This treatment of the Al background is not entirely correct. To apply the proper correction to the extracted longitudinal electron asymmetry (Sec. 4.6.2), the light yield from electrons scattering off the aluminum and the asymmetry they carried would have to be known. The aluminum light yield fraction purely from electron scattering was known from simulation. The problem was that in the data, the measured asymmetry on aluminum was derived from *all* processes originating at the aluminum, including

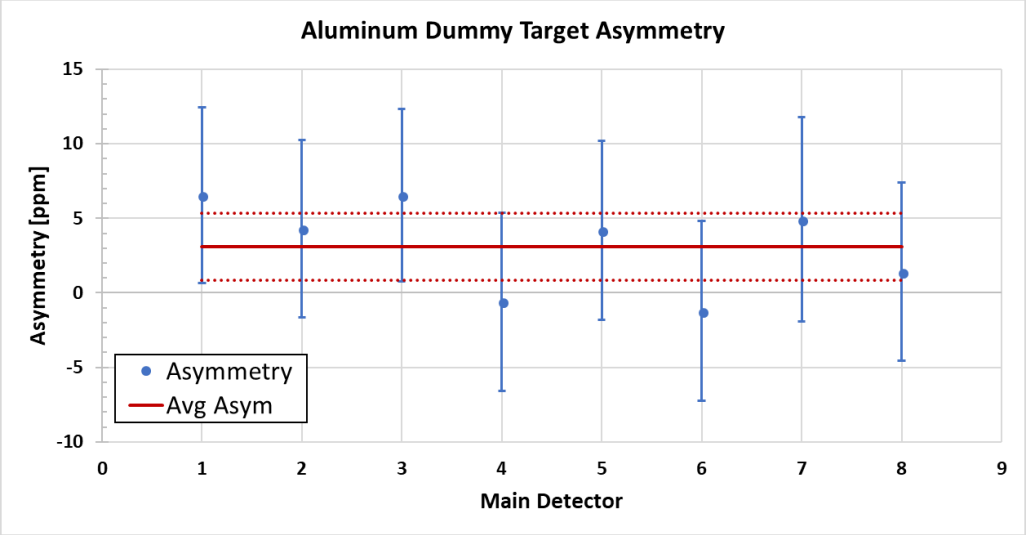

Figure 4.9: Plot of measured regression-corrected asymmetries off of the Al dummy target. The error-weighted average asymmetry (solid red line) and its uncertainty (dotted red lines) excludes MD7.

both pions and electrons, rather than exclusively electrons. Ideally, the asymmetry arising from the electrons would be isolated from the pion asymmetry, but there was not enough statistical power in the aluminum dummy target data to do so.

The average measured aluminum asymmetry was used as an approximation of the true correction, even though it contained contributions from pions. Recall that MD7 was much more sensitive to pions than electrons, due to the lead wall installed on its upstream face. This means that examining the measured asymmetry in MD7 will give an indication of the size of the asymmetry contribution from pions in the other unblocked main detectors.

The asymmetry measured in MD7 was not significantly different than the other main detectors (see Fig. 4.9). It follows that the aluminum asymmetry contribution from pions was similar to the contributions from electrons. Therefore, substituting the average measured aluminum dummy target asymmetry for the asymmetry solely from electrons scattering off of aluminum was a reasonable approximation. Nevertheless, the uncertainty of the average measured asymmetry was increased by 100%, from $\pm 2.2\,\text{ppm}$ to $\pm 4.4\,\text{ppm}$, to account for any possible deviations.

4.4.4 Beamline Background

The tungsten plug (Sec. 3.5) was installed to block the majority of electrons that scattered at very forward angles, that could then interact with the beamline. However, the outer part of the beam, called the beam 'halo', interacted with both the tungsten plug and the beamline, resulting in the beamline background [57].

In the weak charge measurement, the events from the beamline background caused a strong correlation between the main detector asymmetry and the asymmetry measured in the various background detectors, in particular, the US Lumis [1]. The fractional contribution of the Run 2 data collection period of the weak charge measurement was, $f_2 = 0.0019 \pm 0.0004$ [57].

In the work presented here, the correlation is not as distinct (see Fig. 4.10), with a correlation slope of $C_{BB} = 0.40 \pm 0.99\,\text{ppm/ppm}$. The average asymmetry measured by the US Lumis during this data set was, $A_{USL}^{Avg} = 0.16 \pm 0.016\,\text{ppm}$. The fractional light yield for the beamline background determined for the weak charge measurement was modified and used as a rough estimate of the beamline background fraction for the inelastic measurement presented here.

The beamline background rate originates from the beamline, so it is largely independent of the rate of particles that traverse the collimation system. It can be assumed that while the *rate* of beamline background signal will be approximately the same between the weak charge measurement and the inelastic measurement, the signal *fraction* will differ and depend on the rates of other processes.

The total signal rates in the main detectors are approximately two orders of magnitude lower in the inelastic measurement, compared to the weak charge measurement. Therefore, the beamline background signal fraction should be approximately two orders of magnitude larger for the inelastic measurement. This results in an estimated beamline background signal fraction for the inelastic measurement of $f_{BB} = 0.19 \pm 0.19$. To account for all of the approximations involved, a conservative 100% uncertainty was assigned to this value.

The correlation slope, average US Lumi asymmetry, and the estimated background fraction were combined to determine the size of the total beamline background correction that would have to be applied to the extracted longitudinal electron asymmetry,

$$A_{BB} = f_{BB} \cdot C_{BB} \cdot A_{USL}^{Avg} = 0.012 \pm 0.27\,\text{ppm}. \tag{4.43}$$

This correction is negligible when compared to the statistical uncertainty of the extracted asymmetries. For this reason, no actual beamline background correction was applied. Instead, the uncertainty of the extracted longitudinal electron asymmetry, A_e^L, was increased by the 0.27 ppm uncertainty of A_{BB}, by adding them in quadrature.

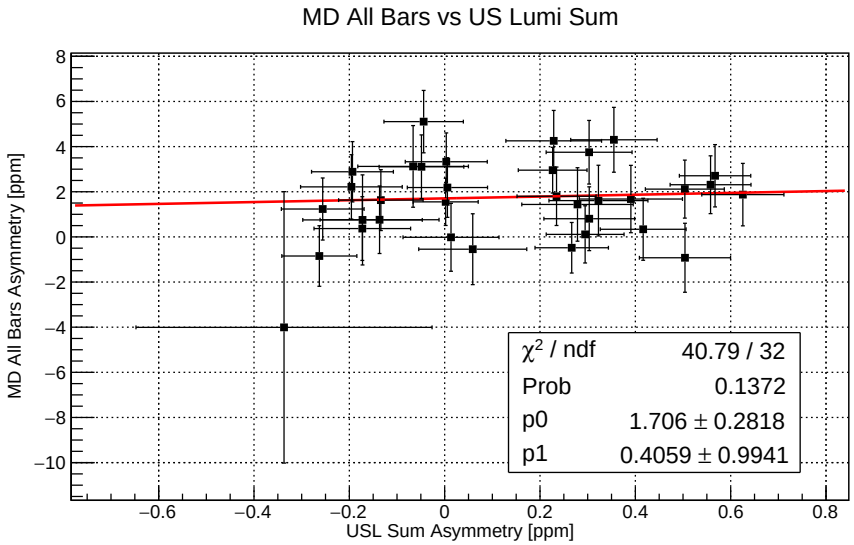

Figure 4.10: Plot of main detector asymmetry versus USLumi asymmetry. Each data point (black square) represents one IHWP state worth of asymmetry data (∼8 h). The linear fit (red line) to the data has a slope of 0.41±0.99 ppm/ppm ($p1$) and an intercept of 1.71±0.28 ppm ($p0$).

4.4.5 Rescattering Bias Effect

The photo-multiplier tube (PMT) double difference (PMTDD) background, or rescattering bias effect, was an unexpected background that was discovered after completion of data collection and after the decommissioning the apparatus. It was found that, as the polarized scattered electrons traversed the magnetic field of QTor, their spins pre-

cessed. This resulted in the electrons having a significant transverse (radial) component upon reaching the MDs.

Lead pre-radiators were installed on the main detectors to suppress the low-energy beamline background (Sec. 4.4.4). Lead has a parity conserving left-right analyzing power. The scattered electrons showered in the lead pre-radiators, resulting in different asymmetries being measured in the two PMTs of each MD.

This was referred to as the PMT double difference and is defined as

$$A_{DD} = A_{-} - A_{+}, \tag{4.44}$$

where $A_{+/-}$ is the measured asymmetry in the '+' or '-' PMTs. The '+' and '-' PMTs are defined as the PMTs on the clockwise and counter-clockwise ends of the MDs, respectively, when facing downstream.

The azimuthally symmetric placement of the MDs and the PMTs on each MD resulted in the cancellation of A_{DD}, to first order. This cancellation was not perfect, because the MDs were not 100% identical and had individual optical response functions. This broken symmetry resulted in imperfect cancellation and caused a bias. The resulting false asymmetry was referred to as A_{bias}.

For the primary $\mathrm{Q_{weak}}$ result, the PMTDD was measured to be, $A_{DD}^{Qweak} = 293 \pm 6$ppb [58].

Thorough GEANT4 simulations of the transport of the detected electrons through the magnetic field of QTor and the Pb pre-radiator were performed. The resulting rescattering bias was calculated to be, $A_{bias}^{Qweak} = 4.3 \pm 3.0$ ppb[1] (see [58] for a detailed description). The same detailed simulations were not necessary and, therefore, not performed at the $\mathrm{Q_{weak}}$ inelastic kinematics. The lower statistics of the inelastic result presented here and the difference in relative size of the PMTDD correction to the size of the final measured asymmetry of interest, made this unnecessary.

In contrast to the primary $\mathrm{Q_{weak}}$ measurement, in the $\mathrm{Q_{weak}}$ inelastic data set presented here, the PMTDD was measured to be, $A_{DD} = 1.3 \pm 0.3$ ppm (see Fig. 4.11).

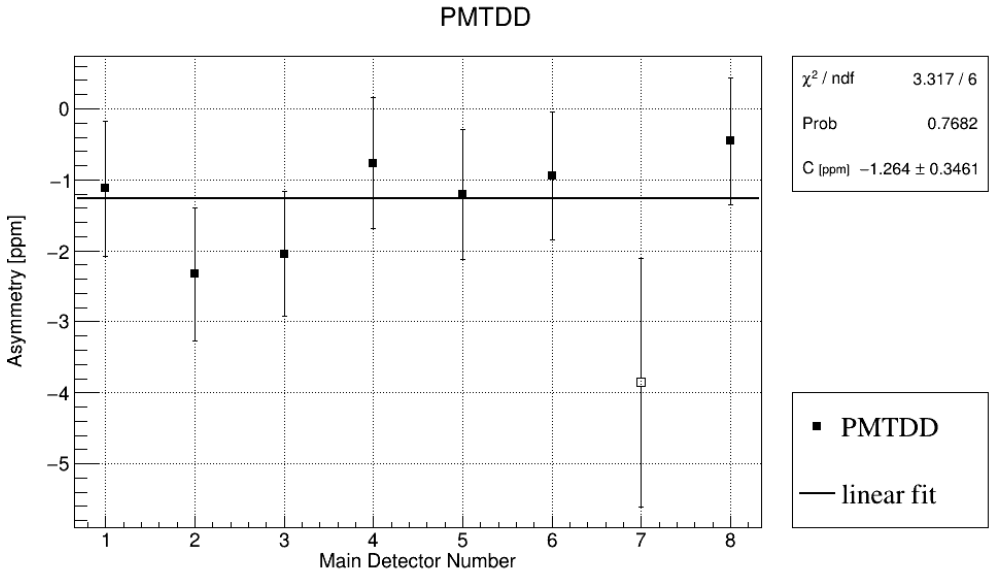

Figure 4.11: Plot of measured PMTDD versus main detector number. Main detector 7 (open square) was excluded from the constant fit (solid black line). Note that asymmetries plotted here should have their signs reversed, because the reversed definition of the PMTDD asymmetry defined in Eq. 4.44 was used in this plot.

The PMTDD calculated here is approximately 4 times the PMTDD calculated for the Q_{weak} primary result. A reasonable estimate of the A_{bias} correction for the inelastic result would then be

$$A_{bias} = \frac{A_{DD}}{A_{DD}^{Qweak}} A_{bias}^{Qweak} = 19 \pm 14\,\text{ppb}. \tag{4.45}$$

The resulting uncertainty on A_{bias} was further increased by a factor of two. This was done to account for the possibility of additional false asymmetries arising from the partially transverse, incident electron beam. Therefore, for this experiment $A_{bias} = 19 \pm 28\,\text{ppb}$.

Even with this inflated uncertainty, the uncertainty of the A_{bias} correction was so negligible that it had no effect on any of the significant digits in the uncertainty of final asymmetry of interest.

A clear understanding of this correction was vital for achieving the precision goals of the primary Q_{weak} result. While it is an arguably unnecessary correction for the

present analysis, it is included here for the sake of completeness.

4.5 Determination of Q^2 and W

For the main Q_{weak} measurement, Q^2 was measured using the tracking system. The tracking chambers were extended into the path of the scattered electrons, the beam current was reduced, and individual scattering events were measured. The four-momentum transfer, Q^2, was then calculated as

$$Q^2 = 2EE'(1 - \cos\theta), \tag{4.46}$$

where E is the energy of the incoming electron, E' is the energy of the outgoing electron, and θ is the scattering angle.

During the inelastic measurement presented here, the scattered particles were comprised of pions, elastically scattered electrons, and inelastically scattered electrons. The separation of the yield fractions of elastically and inelastically scattered electrons required simulation (see Sec. 4.4.2). As such, the method described above could not be used to isolate the inelastically scattered electrons, because the tracking system cannot distinguish between elastically and inelastically scattered electrons. However, the tracking system measured the combined elastic and inelastic Q^2 to be

$$Q^2_{data} = 0.0762 \text{ (GeV)}^2. \tag{4.47}$$

The determination of the inelastic Q^2 was reliant on simulation. The event generator used to calculate the inelastic cross section (described in Sec. 4.4.2) included the effects of internal and external radiation in the target. For a given scattering angle and scattering energy exiting the target, the total cross section was calculated by integrating over the possible radiative processes that could result in those kinematics. These cross sections were calculated with a program external to the simulation, which returns a total cross section based off of the beam energy entering the target and the

scattering energy and scattering angle exiting the target.

As a consequence of the vertex kinematics being integrated over, they cannot be accessed. This results in Q^2 at the vertex also remaining inaccessible. The 'observed', or 'effective', Q^2 was calculated as

$$Q^2 = 2E_{beam}E'_{eff}(1 - \cos\theta_{eff}), \tag{4.48}$$

where E_{beam} is the energy of the electron beam entering the target, and E_{eff} and θ_{eff} are the energy and angle of the scattered electrons, respectively, upon exiting the target.

The inelastic Q^2 was simulated to be

$$Q^2_{inel} = 0.082 \text{ (GeV)}^2. \tag{4.49}$$

The combined elastic and inelastic Q^2 was simulated to be

$$Q^2_{sim} = 0.0787 \text{ (GeV)}^2, \tag{4.50}$$

which deviates from the Q^2 from data, Q^2_{data}, by 2.6 %. This relative difference was used as a conservative uncertainty on the inelastic Q^2, giving a value of

$$Q^2_{inel} = 0.082 \pm 0.002 \text{ (GeV)}^2. \tag{4.51}$$

The energy of the final excited hadronic state, or invariant mass W, is calculated as

$$W^2 = m_A^2 + 2m_A(E - E') - Q^2, \tag{4.52}$$

where m_A is the mass of the target in the initial state. From simulation, the invariant mass for inelastic scattering was determined to be

$$W = 2.23 \pm 0.06 \text{ GeV}. \tag{4.53}$$

4.6 Calculating the Parity-Violating Electron Asymmetry

With eight main detectors and two run types (production and transverse), there were sixteen total raw asymmetries measured from the integrating mode data. The sixteen raw asymmetries, A_{raw}^{ij}, were formed using the normalized yield difference of Eqn. 3.1 over the sum of the PMT signals, where i is the MD number and j is the run type (production or transverse).

4.6.1 Corrections for False Asymmetries

Parity-violating experiments are especially sensitive to the natural, subtle shifts in the position, angle, and energy of the incident beam. If these shifts are correlated with the helicity reversal, they manifest as false asymmetries in the detectors.

Examination of detector sensitivities to normal random beam motion were performed. All raw asymmetries were corrected, through a linear regression scheme, for the natural changes in beam position and angle at the target, as well as beam energy [57]. The regressed asymmetries, A_{reg}^{ij}, were the result of applying the regression corrections to A_{raw}^{ij}. These corrections were typically small (< 0.1 ppm), see Table 4.1. The uncertainty on this regression correction is negligible. Note that the uncertainty on all asymmetries remain unchanged, to two significant figures, when going from A_{raw}^{ij} to A_{reg}^{ij}.

The corrections for the false asymmetries arising from the beamline background (Sec. 4.4.4) and PMT double difference (Sec. 4.4.5) were applied to A_{reg}^{ij} to form the measured asymmetries (see Fig. 4.12),

$$A_{meas}^{ij} = A_{reg}^{ij} + A_{BB} + A_{bias} + A_{blind}. \tag{4.54}$$

The additional term, A_{blind}, was a blinding factor designed to ensure an unbiased analysis of the main Q_{weak} experiment's data. The blinding factor was a single fixed

Main Detector	Raw Asymmetry [ppm]	Uncertainty [ppm]	Regressed Asymmetry [ppm]	Uncertainty [ppm]
1	2.28	0.57	2.24	0.57
2	2.24	0.57	2.24	0.57
3	3.17	0.56	3.19	0.56
4	2.54	0.58	2.58	0.58
5	2.11	0.58	2.10	0.58
6	-0.35	0.58	-0.16	0.58
7	-1.07	0.95	-1.07	0.95
8	1.46	0.57	1.49	0.57

Table 4.1: PMT averaged asymmetries for each main detector from the production data set. Raw asymmetries, A_{raw}^{ij}, as well as the regression-corrected asymmetries, A_{reg}^{ij}, are shown. Note that all corrections were less than 0.20 ppm and they caused no appreciable increase in uncertainty.

asymmetry value that was applied as an offset to the entire data set, randomized between -60 ppb and 60 ppb. Its value was unknown until analysis was complete, which masked the true value of the measured asymmetries. This range was constructed for blinding the main Q_{weak} experiment's precision asymmetry measurements, which were expected to be on the order of a few hundred ppb with an uncertainty on the order of ten ppb. However, this range was inadequate for blinding the inelastic measurement presented here, because the asymmetry was expected to be on the order of ten ppm with an uncertainty on the order of a few ppm. During this data collection period, the blinding factor was 6.669 ppb, which was negligible compared to the measured asymmetries.

4.6.2 Asymmetry Parameterization

Ideally, data would have been collected using a 100% longitudinally polarized beam and using a detector system that could veto all scattered particles except electrons. The resulting measured asymmetries, A_{meas}^{ij} from Eqn. 4.54, would then be entirely due to the parity-violating asymmetry from scattered electrons.

The actual experimental conditions were far from ideal, due to the partially transverse electron beam and a large background from pions. To proceed with the

analysis, the parity-violating asymmetry from scattered electrons needed to be isolated from all other processes. This included separating the longitudinal and transverse asymmetries, as well as, separating the effect of electrons from pions.

The beam polarization angle was a measure of the angle of the beam electrons' polarization vectors relative to the beam axis, in the horizontal plane. A polarization angle of 0° ($\theta_P = 0°$) is defined to be parallel to the beam axis and pointing downstream. These polarization vectors can be parameterized in terms of a 'longitudinal' component parallel to the beam axis, and a 'transverse' component orthogonal to the beam axis in the horizontal plane. The longitudinal and transverse components resulted in an associated 'longitudinal' or 'transverse' asymmetry, respectively.

The beam polarization angle was different for the two run types, where production runs had a beam polarization angle of $-19.7° \pm 1.9°$ and transverse runs had an angle of $92.2° \pm 1.9°$ (As discussed in Sec. 4.1.2). As a consequence, the measured asymmetries for the different run types each contain component asymmetries derived from a different linear combination of the longitudinal and transverse asymmetries. Therefore, those individual longitudinal and transverse asymmetries can be disentangled and separated from each other.

Likewise, the lead wall attenuating the electrons in MD7 led to different ratios of pions to electrons being detected in MD7 versus the other unblocked main detectors (Sec. 4.2.1 & Sec. 4.2.2). Therefore, the regression-corrected measured asymmetries, A^{ij}_{meas}, could be parameterized according to source particle type and polarization component, where i is the main detector number (1-8) and j is the run type (production or transverse). The neutral background, discussed in Sec. 4.3, dilutes the asymmetries measured in the detectors and must also be accounted for. The effect in each MD is corrected for with the addition of a scaling factor, $(1 - f^i_{NB})$.

The measured asymmetries were therefore parameterized as follows,

$$A^{ij}_{meas} = (1 - f^i_{NB})\Big[(1 - f^{avg/7}_{\pi})(A^L_e \cos\theta^j_P + A^T_e \sin\theta^j_P \sin\phi^i) + f^{avg/7}_{\pi}(A^L_{\pi} \cos\theta^j_P + A^T_{\pi} \sin\theta^j_P \sin\phi^i)\Big]. \quad (4.55)$$

The fractional yield from pions seen in MD7 is represented by f^7_{π}. The average fractional yield seen by the seven unblocked main detectors is f^{avg}_{π}. The longitudinal asymmetry from electrons(pions) is $A^L_{e(\pi)}$. The transverse asymmetry from electrons(pions) is $A^T_{e(\pi)}$. The polarization angle of run type j is θ^j_P. The neutral background yield fraction for MD i is f^i_{NB}. The fixed angles corresponding to the azimuthal angle placement of the main detectors are ϕ^i, with $\phi^1 = 0°$, $\phi^2 = 45°$, etc.

4.6.3 Component Asymmetry Separation

To extract the component asymmetries, A^L_e, A^T_e, A^L_{π}, and A^T_{π}, from the regression-corrected measured asymmetries in Eq. 4.55, a 'Many-Worlds' Monte-Carlo minimization approach was implemented. The input quantities to this minimization were A^{ij}_{meas} (Sec. 4.6.1), f^{avg}_{π} (Sec. 4.2.1), f^7_{π} (Sec. 4.2.2), f^i_{NB} (Sec. 4.3), and θ^j_P (Sec. 4.1.2). A value for each input quantity was randomly selected from a Gaussian distribution about their mean with widths equal to their uncertainties. These random values were then used to calculate the asymmetry in each MD and for each polarization configuration via the following equation:

$$A^{ij}_{calc} = (1 - \tilde{f}^i_{NB})\Big[(1 - \tilde{f}^{avg/7}_{\pi})(A^L_e \cos\tilde{\theta}^j_P + A^T_e \sin\tilde{\theta}^j_P \sin\phi^i) + \tilde{f}^{avg/7}_{\pi}(A^L_{\pi} \cos\tilde{\theta}^j_P + A^T_{\pi} \sin\tilde{\theta}^j_P \sin\phi^i)\Big], \quad (4.56)$$

where a '$\sim$' over a quantity indicates a randomly selected value for that quantity. The function δ, where

$$\frac{\delta^2}{dof} = \sum(\tilde{A}^{ij}_{meas} - A^{ij}_{calc})^2, \quad (4.57)$$

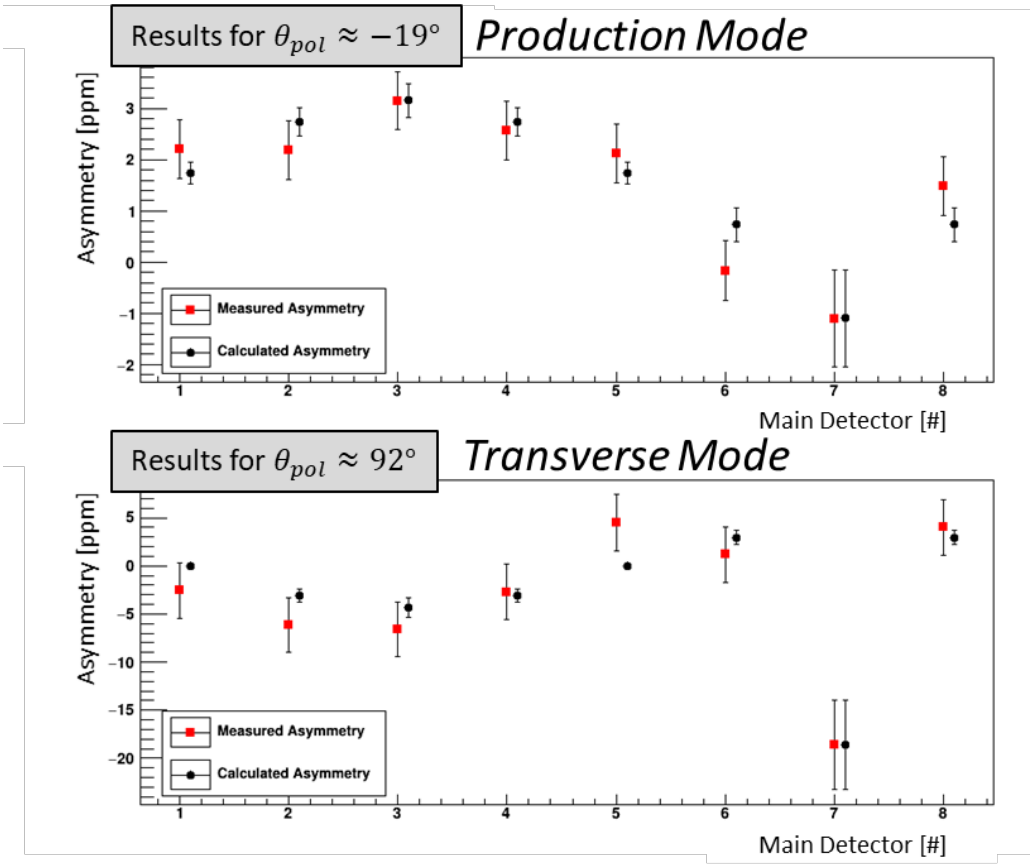

Figure 4.12: Plots of measured (red squares) and calculated (black circles) asymmetries vs main detector number are shown. The top plot shows the asymmetries for the mixed polarization production mode data set, and the bottom plot shows the asymmetries for the pure transverse data set. Both sets of measured asymmetries show clear sinusoidal dependence and the calculated asymmetries reproduce that dependence. Recall that main detector 7 had the lead wall on its upstream face.

was then minimized with respect to the unknown component asymmetries. This resulted in one possible set of values for each component asymmetry, A_e^L, A_e^T, A_π^L, and A_π^T.

The randomization and minimization process was repeated 10^6 times, giving 10^6 extracted values for each of the four component asymmetries and 10^6 values for the calculated asymmetries (shown in Fig. 4.12). Iterating 10^6 times ensured that each input quantity was sampled sufficiently to span its probability distribution. This large amount of repeated input sampling also ensured that the distributions of extracted

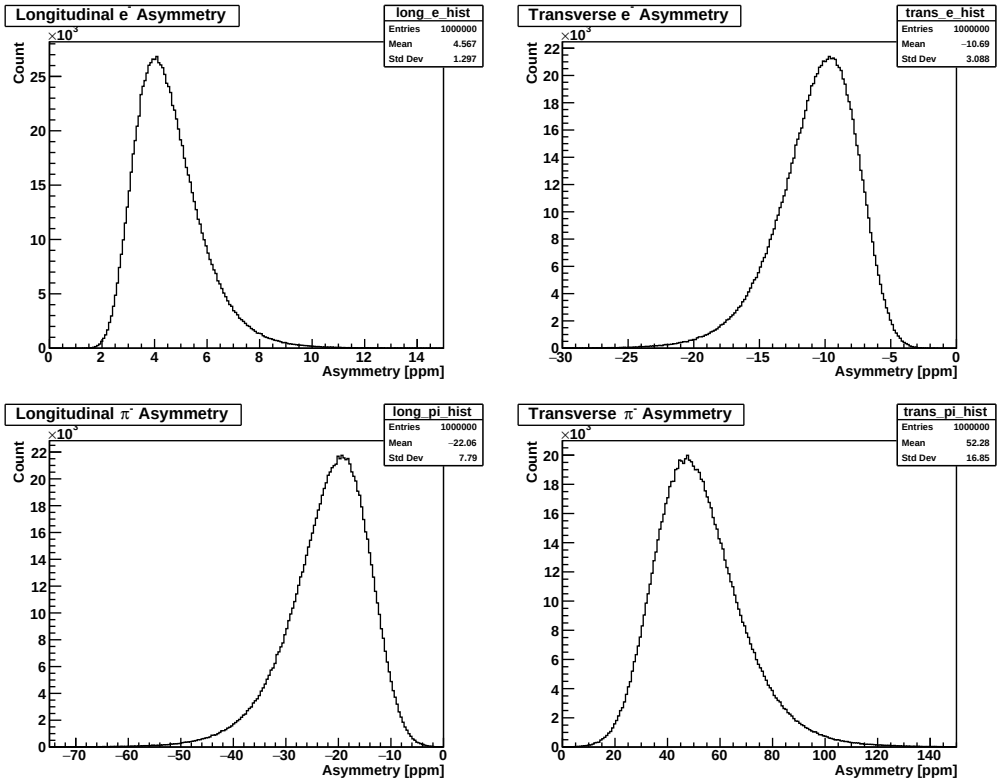

Figure 4.13: The distributions of the four extracted asymmetries from the 'Many-Worlds' Monte-Carlo minimization are shown: asymmetry from electrons arising from longitudinal beam (upper left), asymmetry from electrons arising from transverse beam (upper right), asymmetry from pions arising from longitudinal beam (lower left), and asymmetry from pions arising from transverse beam (lower right). The longitudinal electron asymmetry shown contains the combined contributions from both elastically and inelastically scattered electrons, as well as backgrounds that haven't been corrected for at this stage of the analysis (Sec. 4.4). Note that there is an overall sign difference between these histograms and the asymmetries listed in Tab. 4.2, due to the sign of the overall beam polarization not being corrected for yet. The correct signs are those listed in Tab. 4.2.

component asymmetries were smooth (see Fig. 4.13).

The root mean squared (RMS) of the resulting distributions are taken as their uncertainties. Additionally, any correlated uncertainties on the input quantities are automatically accounted for in the uncertainties of the extracted asymmetries in this 'Many-Worlds' approach.

Each input quantity had a contribution to the uncertainties of the extracted asymmetries. To separate the contributions, the whole calculation was repeated, but

Asymmetry	Mean[ppm]	RMS[ppm]
A_e^L	-4.57	1.30
A_e^T	10.69	3.09
A_π^L	22.06	7.79
A_π^T	-52.28	16.85

Table 4.2: Asymmetries extracted from the 'Many-Worlds' Monte-Carlo minimization process. Quoted in the table above are the means and RMS's of the distributions in Fig. 4.13.

with all input uncertainties 'turned off' except one. For example, to calculate the contribution of the uncertainty in $f_\pi^{avg/7}$ to the final uncertainties of the component asymmetries, the uncertainties on A_{meas}^{ij} and θ_P^j were set to zero and the minimization process was repeated. The resulting uncertainty on the extracted asymmetries is then due solely to the effect of the uncertainty of $f_\pi^{avg/7}$. Each input quantity (A_{meas}^{ij}, $f_\pi^{avg/7}$, f_{NB}^i, and θ_P^j) received a similar treatment. The neutral background fraction for MD7, f_{NB}^7, was examined separately from the other MDs, because of its much larger uncertainty.

The statistical uncertainty was determined by subtracting, in quadrature, the relative uncertainty of the false asymmetry corrections, in Eqn. 4.54, from the relative uncertainty of the measured asymmetries. The result was then multiplied by the uncertainty contribution of the measured asymmetries on the uncertainty of A_e^L,

$$\sigma_{stat} = \sigma_{A_e^L}^{meas} \sqrt{\left(\frac{\sigma_{A_{meas}}}{A_{meas}}\right)^2 - \left(\frac{\sigma_{A_{BB}}}{A_{BB}}\right)^2 - \left(\frac{\sigma_{A_{bias}}}{A_{bias}}\right)^2}, \tag{4.58}$$

where σ_{stat} is the statistical uncertainty of A_e^L, $\sigma_{A_e^L}^{meas}$ is the uncertainty contribution of the measured asymmetries on the uncertainty of A_e^L, and σ_{A_k} is the uncertainty on A_k for $k = [meas, BB, bais]$.

The resulting four component asymmetries extracted from the measured asymmetries are summarized in Table 4.2.

Chapter 5

Results and Discussion

5.1 Results

The inelastic asymmetry result presented here, was a challenging ancillary measurement of the Q_{weak} experiment. The goal of this measurement was to provide additional data to constrain theoretical models of the electroweak interference structure functions.

5.1.1 Extracting the Inelastic Asymmetry

The physics asymmetry of interest (inelastic $\vec{e}p$) was contained within the longitudinal electron asymmetry, A_e^L, determined in Sec. 4.6.3. Corrections for background processes, as well as the overall polarization of the beam were applied to A_e^L to determine the physics asymmetry using

$$A_{phys} = \frac{A_e^L/P - \sum^k f_k A_k}{1 - \sum^k f_k}, \tag{5.1}$$

where P is the total polarization of the electron beam and $k = [El, PT, Al]$.

5.1.2 Final Inelastic Asymmetry Measurement

With all backgrounds having been measured or simulated, the final parity-violating asymmetry from inelastic electron-proton scattering can now be extracted from Eqn. 5.1.

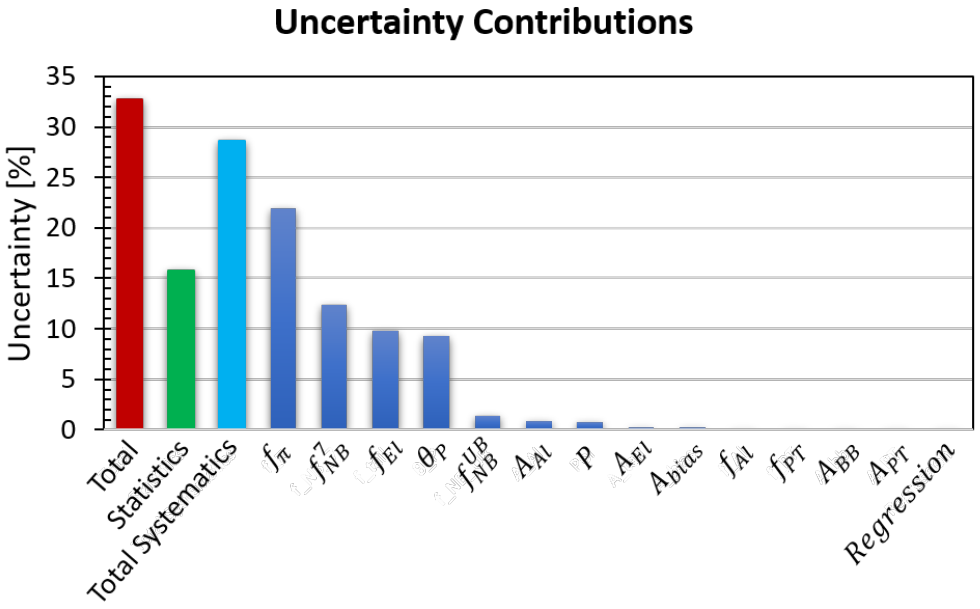

Figure 5.1: Visualization of all uncertainty contributions to A_{phys}. The total systematic uncertainty (cyan bar) is the quadrature sum of the individual systematic uncertainties (blue bars). The total uncertainty (red bar) is systematics-dominated, with the determination of the pion yield fraction as the largest single source of uncertainty.

This physics asymmetry was determined to be

$$A_{phys} = -13.5 \pm 2.0(statistical) \pm 3.9(systematic)\text{ppm} \tag{5.2}$$

$$= -13.5 \pm 4.4(total)\text{ppm} \tag{5.3}$$

at $Q^2 = 0.082\,\text{GeV}^2$ and $W = 2.23\,\text{GeV}$. This is a $\sim 33\%$ precision measurement of the inelastic parity-violating asymmetry. The final uncertainty is dominated by systematic uncertainties, the largest of which arises from the determination of the fractional yield originating from pions.

5.1.3 Summary of Uncertainty Contributions

The uncertainty of the final inelastic PV asymmetry was dominated by systematic uncertainties (28.7% relative) (see Tab. 5.1). The four primary contributors, in decreasing order of size, were the pion yield fraction, determination of the neutral

Quantity	Label	Value	Contribution to ($\frac{dA_{phys}}{A_{phys}}$)
Pion Yield Fraction	f_π^{avg}	0.096 ± 0.029	21.9%
	f_π^7	0.81 ± 0.05	
Neutral Background in MD7	f_{NB}^7	0.51 ± 0.09	12.4%
Elastic Radiative Tail Yield Fraction	f_{El}	0.62 ± 0.04	9.8%
Polarization Angle	θ_P^{Prod}	$-19.7^\circ \pm 1.9^\circ$	9.3%
	θ_P^{Trans}	$92.2^\circ \pm 1.9^\circ$	
Neutral Background in Unblocked MDs	f_{NB}^{UB}	0.063 ± 0.006	1.4%
Aluminum Window Asymmetry	A_{Al}	-3.1 ± 2.2ppm	0.9%
Beam Polarization	P	$87.0 \pm 0.6\%$	0.8%
Elastic Radiative Tail Asymmetry	A_{El}	0.58 ± 0.02ppm	0.3%
Rescattering Bias Effect	A_{bias}	19 ± 14ppb	0.2%
Aluminum Window Yield Fraction	f_{Al}	0.0075 ± 0.0009	0.2%
Punch-Through Yield Fraction	f_{PT}	0.0220 ± 0.0007	$< 0.1\%$
Beamline Background Asymmetry	A_{BB}	0.012 ± 0.27ppm	$< 0.1\%$
Punch-Through Asymmetry	A_{PT}	-3.96 ± 0.04ppm	$< 0.1\%$
Regression Correction		$< 0.20 \pm 0.00$ppm	$< 0.1\%$
Total Systematics			28.7%
Statistics			15.8%
Total:			**32.8%**

Table 5.1: Summary of contributions to the uncertainty on A_{phys}, in relative percent.

background in MD7, elastic radiative tail yield fraction, and polarization angle of the electron beam.

The pion yield fraction represented the largest contribution of uncertainty (21.9% relative). This uncertainty arose due to challenges in separating integrated signals in the main detectors, where both electrons and pions were measured indiscriminately (Sec. 4.2.1).

The second largest systematic uncertainty was the neutral fraction in MD7 (12.4% relative). Due to the presence of a lead wall, MD7 had significantly lower event rates than the other MDs, resulting in a much larger neutral yield fraction in MD7. Due to the lack of direct measurement of the neutral background in MD7, determination of the neutral background yield fraction in this MD was reliant on simulation, resulting in a large uncertainty (Sec. 4.3).

The elastic radiative tail background yield fraction was a very large correction

(Sec. 4.4.2). The yield in the main detectors arising from the elastic radiative tail was almost twice the yield from the inelastic signal of interest. As such, simulation was needed to separate the elastic and inelastic yield signals in the main detectors. This separation resulted in a 9.8% relative uncertainty on the inelastic asymmetry.

Lastly, uncertainty in the polarization angle was the fourth largest contribution (9.3% relative) to the overall systematic uncertainty in this measurement. The transverse component arose due to mixing of longitudinally and transversely polarized electrons in the electron beam (Sec. 4.1.2). The contribution of the longitudinal component was separated from the mixed polarization data through a Monte-Carlo 'many-worlds' approach (Sec. 4.6.2).

The remaining systematic uncertainties were almost negligible (each less than 1.5% relative) in comparison to the four primary systematic uncertainties and in comparison to the statistical uncertainty (15.8% relative) (see Fig. 5.1).

Potential methods of mitigating the four leading systematic uncertainties are discussed in Sec. 5.2.1.

5.1.4 Comparison with Theoretical Predictions

The evolution of the inelastic PV asymmetry from electron-proton scattering was provided by [25] (see Fig. 5.2), using theory predictions for $\Box_{\gamma Z}$. Two models, the Adelaide-Jefferson Lab-Manitoba (AJM) model [25] and Gorchtein, Horowitz, and Ramsey-Musolf (GHRM) model [7], agree on the central value for the kinematic region of the inelastic PV asymmetry. Where they differ is in their treatments of the uncertainties of some of the input parameters to the calculations. See [25] for a detailed description of these differences.

The asymmetry measured here, $A_{Phys} = -13.5 \pm 4.4\,\text{ppm}$, is in agreement with

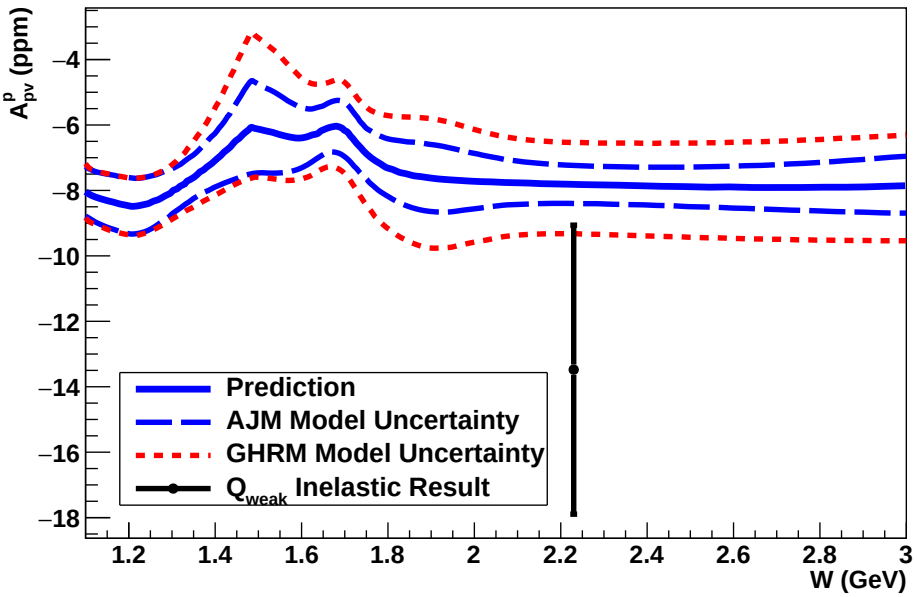

Figure 5.2: Theoretical prediction of the inelastic PV asymmetry versus W, at fixed $Q^2 = 0.9\,\mathrm{GeV}^2$ (solid blue line). The AJM model [25] uncertainties (blue dashed line) are shown along with the GHRM model [7] uncertainties (red dotted line). The result from this experiment (black circle) is at a slightly smaller $Q^2 = 0.082 \pm 0.004\,\mathrm{GeV}^2$, and lies in the non-resonant, or continuum, region of this predicted asymmetry. Reproduced from [25] and modified.

both the AJM and GHRM predictions [25],

$$A^p_{PV}(AJM) = -7.8 \pm 0.6\,\mathrm{ppm} \tag{5.4}$$

$$A^p_{PV}(GHRM) = -7.8 \pm 1.5\,\mathrm{ppm}. \tag{5.5}$$

These asymmetries follow directly from predictions of $\Box_{\gamma Z}$.

5.2 Discussion

Typically, experiments performed at accelerator facilities are planned many months or years ahead of actual data collection. The $\mathrm{Q_{weak}}$ inelastic measurement presented here is not typical. It was an opportunistic measurement performed during a period of time that another experiment hall at Jefferson Lab had priority in selecting the

properties of the electron beam. Despite a short planning cycle, the collaboration was able to leverage the apparatus to make a measurement that was not only useful to the main experiment, but also contained interesting physics that could stand on its own.

The Q_{weak} inelastic result, presented here, provides useful experimental data in a kinematic region where little to no data exists (see Sec. 2.3.2). Recall from Sec. 2.3.1, that $\Box_{\gamma Z}$ can be separated into a vector piece, $\Box^V_{\gamma Z}$, and an axial piece, $\Box^A_{\gamma Z}$. The most important inputs into the calculations of $\Box^V_{\gamma Z}$ are the interference structure functions, $F_1^{\gamma Z}$ and $F_2^{\gamma Z}$. The Q_{weak} inelastic result, described in this dissertation, can be used to experimentally constrain the γZ structure functions, leading to an increased understanding of proton structure.

Additionally, a correction for $\Box_{\gamma Z}$ was necessary for the main Q_{weak} result, a precision measurement of the weak charge of the proton [1]. The integrals over kinematic variables, W^2 and Q^2, that were necessary to calculate this correction were dominated by Region I in Fig. 2.7. The inelastic result presented here in this dissertation, lies within Region I, and agrees with the theoretical prediction. The inelastic result was not used to directly make a correction to the main Q_{weak} experimental result. Instead this inelastic measurement provides important experimental validation of the models and adds further confidence in the $\Box_{\gamma Z}$ correction applied to the main Q_{weak} result.

Further, this result can reduce the uncertainty on $\Box_{\gamma Z}$ radiative corrections. Better understanding of these radiative corrections allows for more precise measurements in future experiments, such as MOLLER at Jefferson Lab [28] and P2 at MESA [27].

5.2.1 Improving Systematic Uncertainties

With more time to plan, and a healthy budget for hardware, many of the systematic uncertainties in the Q_{weak} inelastic measurement could have been drastically reduced. The four primary sources of systematic uncertainty are discussed in Sec. 5.1.3. Methods that could be used to reduce each of these uncertainties will be addressed in turn.

The pion yield fraction uncertainty was the largest systematic uncertainty and would therefore be the most important to improve upon. The 'pion detector' used for

this measurement was very crude and consisted of a wall of lead bricks placed on the upstream face of one of the main detectors (Sec. 3.4.2). A better method of particle identification was needed.

With that in mind, an Aerogel and Lead glass detector combination was installed and operated during data collection, with the goal of measuring the pion yield fraction. A malfunction in DAQ electronics that affected the Aerogel and Lead glass detectors was not discovered until after the completion of the experiment. This malfunction rendered these detectors all but useless. If this second method of measuring the pion yield fraction had not malfunctioned, it could have served as a useful cross check of the pion fraction determined with the crude lead wall. Both methods together would have greatly reduced the uncertainty of the pion background measurement.

Another method of identifying the pion background would involve the addition of gas Cerenkov detectors. These gas Cerenkov detectors would be placed just upstream of the existing quartz Cerenkov detectors. Gas Cerenkov detectors allow for calibration of the thresholds of their PMTs such that they are insensitive to pions. With appropriate threshold settings for both sets of detectors, the pion yield fraction could be more precisely determined.

The next largest systematic uncertainty was the determination of the neutral yield fraction in MD7. There was no dedicated measurement of the neutral yield fraction in MD7. Lacking an actual measurement, simulation was needed to estimate the size and uncertainty of the neutral background in MD7.

With even a short data collection run, this uncertainty could have been greatly reduced by rotating the tracking system in front of MD7 to measure neutral particles directly. This configuration would allow the trigger scintillator to be used to veto charged particles using the same method as the other main detectors (Sec. 4.3), and thereby eliminating the reliance on simulation. Unfortunately, the lead wall blocked the rotation system from reaching that configuration.

Achieving this configuration may have been possible, albeit tricky. Executing that configuration would have required disassembly of the lead wall, rotation of the tracking

system, and careful reconstruction of the lead wall in the narrow space between the tracking system and main detector. After a specialized data collection run to determine the neutral yield fraction in MD7, the configuration would require careful disassembly in order to revert back to the original configuration.

In our ignorance of the magnitude of this uncertainty, this measurement was forgone in favor of other specialized measurements, based on the complicated reconfiguration process. In hindsight, this measurement should have been given a higher priority.

An alternate method of measuring this background could involve the use of several scintillators. Instead of a single scintillator located in the path of scattered particles used as a veto, the main detectors could be surrounded by scintillators. These scintillators could be used to veto incident charged particles from all directions. This apparatus change would ensure improved identification of neutral particles. Thus, the uncertainty on the neutral yield fraction would be reduced.

The elastic radiative tail yield fraction and its uncertainty were both large. The uncertainty of this background yield fraction was based off of fits to world data [54]. Barring the addition of more data to significantly improve the fits, the best method to reduce the effect of this background is to reduce the size of the background itself.

The elastically scattered electrons radiated energy through bremsstrahlung radiation when traversing the long primary ℓH_2 target ($\sim 35\,\mathrm{cm}$). A thinner target would reduce the fraction of elastically scattered electrons that radiated sufficient energy to fall into the acceptance of the apparatus. A side effect of a thinner target would be the reduction of statistics. The reduced statistics could be compensated for by either increasing the beam current or increasing the duration of the experiment. Finding the ideal balance of these competing effects would require some study.

Finally, the other large systematic uncertainty, from the mixed polarization angle, has a very simple solution for reducing its effect. The PV inelastic asymmetry originated from the longitudinal component of the beam. Simply having a fully longitudinal beam would have virtually eliminated any uncertainty due to the polarization angle.

5.2.2 Future Work

As parity-violating measurements become increasingly more precise, our understanding of radiative corrections, such as $\Box_{\gamma Z}$, must likewise increase. Being backed by very little data, the $\Box_{\gamma Z}$ provides ample opportunity for further study.

The integrals used in the calculations of $\Box_{\gamma Z}$ cover a wide range in W^2 and Q^2 (see Fig. 2.7). Inelastic data in any of the three integration regions would be useful for constraining the theory.

For any future experiment that requires a $\Box_{\gamma Z}$ correction, the energy of the experiment determines which of the integration regions would need to be most precisely constrained by other data.

For example, for experiments with energy, $E \lesssim 5.0\,\mathrm{GeV}$, such as the $\mathrm{Q_{weak}}$ [1] experiment at Jefferson Lab and the MESA experiment at Mainz [27], the focus should be on data in the low W^2 and low Q^2 region, Region I of Fig. 2.7. At these energies, the uncertainty of the $\Box_{\gamma Z}$ correction is dominated by how well the electroweak interference structure functions are constrained in Region I (see Fig. 2.8). Ideally, a systematic study of PV electron-proton scattering across Region I would be performed. For experiments with higher energies, such as MOLLER [28], Regions II and III become larger contributors to the uncertainty of a $\Box_{\gamma Z}$ correction.

The upcoming SoLiD experiment, at Jefferson Lab, will measure parity-violating deep inelastic scattering on both hydrogen and deuterium targets [59], which has the potential to provide additional data to constrain γZ box calculations.

5.2.3 Final Remarks

This dissertation, as well as future parity-violating inelastic electron-proton scattering experiments, can be used to further refine theoretical models of the γZ box correction. This is an important part of the Standard Model that lacks sufficient experimental backing and is needed to further elucidate the electroweak sector.

As stated, this measurement was ancillary to the main $\mathrm{Q_{weak}}$ experiment. It was

an opportunistic chance to add experimental validation to the γZ box in an unexplored kinematic regime.

This ancillary measurement was the measurement most separate from the main Q_{weak} experiment. The apparatus was not designed for this purpose. It wasn't built for this task. When in need of a hammer, all we had was a wrench.

Without the proper 'tools' and using the apparatus in a manner inconsistent with its design, the resulting large backgrounds became a difficult challenge to the analysis. The compounding effects of each background ultimately resulted in a large, $\sim 33\%$ uncertainty in this measurement.

Despite the challenges of the backgrounds we were able to provide one of the very first parity-violating measurements in this essentially unexplored kinematic regime (i.e. not truly deep inelastic scattering (DIS), but also not elastic or at one of the low-lying resonances). Additionally, we have helped to validate the theoretical description of parity-violating electron scattering (PVES) in these kinematics, and bolstered our confidence in the calculation of electroweak corrections, (e.g. the precision elastic scattering measurements) as well.

References

[1] D. Androić et al. (Qweak), Nature **557**, 207 (2018).

[2] C. Patrignani et al. (Particle Data Group), Chin. Phys. **C40**, 100001 (2016).

[3] J. Erler, A. Kurylov, and M. J. Ramsey-Musolf, Phys. Rev. **D68**, 016006 (2003).

[4] N. L. Hall, P. G. Blunden, W. Melnitchouk, A. W. Thomas, and R. D. Young, Phys. Lett. **B753**, 221 (2016).

[5] P. G. Blunden, W. Melnitchouk, and A. W. Thomas, Phys. Rev. Lett. **107**, 081801 (2011).

[6] P. G. Blunden, W. Melnitchouk, and A. W. Thomas, Phys. Rev. Lett. **109**, 262301 (2012).

[7] M. Gorchtein, C. J. Horowitz, and M. J. Ramsey-Musolf, Phys. Rev. **C84**, 015502 (2011).

[8] M. Tanabashi et al. (Particle Data Group), Phys. Rev. D **98**, 030001 (2018).

[9] A. D. Sakharov, Pisma Zh. Eksp. Teor. Fiz. **5**, [Usp. Fiz. Nauk161,no.5,61(1991)], 32 (1967).

[10] I. Newton, *Philosophiae naturalis principia mathematica* (J. Societatis Regiae ac Typis J. Streater, 1687).

[11] E. Noether, Nachrichten von der Königl. Gesellschaft der Wissenschaften und der Georg-Augusts-Universitt zu Göttingen, Mathematisch-Physikalische, 235 (1918).

[12] S. L. Glashow, J. Iliopoulos, and L. Maiani, Phys. Rev. **D2**, 1285 (1970).

[13] S. Weinberg, Phys. Rev. Lett. **19**, 1264 (1967).

[14] A. Salam, Conf. Proc. **C680519**, 367 (1968).

[15] P. W. Higgs, Phys. Rev. Lett. **13**, 508 (1964).

[16] F. Englert and R. Brout, Phys. Rev. Lett. **13**, 321 (1964).

[17] L. W. Mo and Y.-S. Tsai, Rev. Mod. Phys. **41**, 205 (1969).

[18] Y.-S. Tsai, *Radiative corrections to electron scatterings*, (1971) `http://www.slac.stanford.edu/cgi-wrap/getdoc/slac-pub-0848.pdf`.

[19] W. J. Marciano and A. Sirlin, Phys. Rev. **D27**, 552 (1983).

[20] W. J. Marciano and A. Sirlin, Phys. Rev. **D29**, [Erratum: Phys. Rev.D31,213(1985)], 75 (1984).

[21] M. J. Musolf and B. R. Holstein, Phys. Lett. **B242**, 461 (1990).

[22] M. Gorchtein and C. J. Horowitz, Phys. Rev. Lett. **102**, 091806 (2009).

[23] A. Sibirtsev, P. G. Blunden, W. Melnitchouk, and A. W. Thomas, Phys. Rev. **D82**, 013011 (2010).

[24] B. C. Rislow and C. E. Carlson, Phys. Rev. **D88**, 013018 (2013).

[25] N. L. Hall, P. G. Blunden, W. Melnitchouk, A. W. Thomas, and R. D. Young, Phys. Rev. **D88**, 013011 (2013).

[26] J. Arrington, P. G. Blunden, and W. Melnitchouk, Prog. Part. Nucl. Phys. **66**, 782 (2011).

[27] F. Hug, K. Aulenbacher, R. Heine, B. Ledroit, and D. Simon, in Proceedings, 28th International Linear Accelerator Conference (LINAC16): East Lansing, Michigan, September 25-30, 2016 (2017), MOP106012.

[28] J. Benesch et al. (MOLLER), arXiv:1411.4088v2 (2014).

[29] D. Androic et al. (G0), (2012).

[30] D. Wang et al. (Jefferson Lab Hall A), Phys. Rev. Lett. **111**, 082501 (2013).

[31] D. Wang et al., Phys. Rev. **C91**, 045506 (2015).

[32] T. Allison et al. (Q_{weak} Collaboration), Nuclear Instruments and Methods in Physics Research Section A: Accelerators, Spectrometers, Detectors and Associated Equipment **781**, 105 (2015).

[33] D. Androic et al. (Q_{weak} Collaboration), Physical Review Letters **111**, 141803 (2013).

[34] J. Dudek et al., Eur. Phys. J. **A48**, 187 (2012).

[35] C. W. Leemann, D. R. Douglas, and G. A. Krafft, Ann. Rev. Nucl. Part. Sci. **51**, 413 (2001).

[36] K. D. Bartlett, "First measurements of the parity-violating and beam-normal single-spin asymmetries in elastic electron-aluminum scattering", PhD thesis (College of William & Mary, 2018).

[37] P. A. Adderley et al., Conf. Proc. **C110328**, 862 (2011).

[38] J. A. Magee et al., Phys. Lett. **B766**, 339 (2017).

[39] M. Hauger et al., Nucl. Instrum. Meth. **A462**, 382 (2001).

[40] A. Narayan et al., Phys. Rev. **X6**, 011013 (2016).

[41] W. M. Yao et al. (Particle Data Group), J. Phys. **G33**, 1 (2006).

[42] J. M. Mammei, "Parity-Violating Elastic Electron Nucleon Scattering: Measurement of the Strange Quark Content of the Nucleon and Towards a Measurement of the Weak Charge of the Proton", PhD thesis (Virginia Polytechnic Institute and State University, 2010).

[43] J. R. Hoskins, "Determination of the proton's weak charge via parity violating e-p scattering", PhD thesis (College of William & Mary, 2015).

[44] J. P. Leckey IV, "The first direct measurement of the weak charge of the proton", PhD thesis (College of William & Mary, 2012).

[45] K. E. Myers, "The first determination of the proton's weak charge through parity-violating asymmetry measurements in elastic e + p and e + al scattering", PhD thesis (The George Washington University, 2012).

[46] M. J. McHugh III, "A Measurement of the Transverse Asymmetry in Forward-Angle Electron-Carbon Scattering Using the Q_{weak} Apparatus", PhD thesis (The George Washington University, 2017).

[47] M. Dalton, *3 pass polarization angle*, QweakELOG, (Dec. 2015) `https://qweak.jlab.org/elog/Ancillary/227`.

[48] D. Gaskell, *Run 2 final polarizations - updated proposal*, QweakELOG, (May 2015) `https://qweak.jlab.org/elog/DAQ+%5C%26+Analysis/334`.

[49] F. James and M. Roos, Comput. Phys. Commun. **10**, 343 (1975).

[50] D. E. Wiser, "Inclusive Photoproduction of Protons, Kaons, and Pions at SLAC Energies", PhD thesis (Wisconsin U., Madison, 1977).

[51] D. Armstrong, *Attempt to get Neutral fraction in MD7 for 3-pass data*, WM Electronic Logbooks for the JLab Parity Experiments, (Mar. 2018) `https://dilbert.physics.wm.edu/Physics/232`.

[52] Y.-S. Tsai, Rev. Mod. Phys. **46**, [Erratum: Rev. Mod. Phys.49,521(1977)], 815 (1974).

[53] J. Schwinger, Phys. Rev. **A24**, 2353 (1981).

[54] M. E. Christy and P. E. Bosted, Phys. Rev. **C81**, 055213 (2010).

[55] S. R. Dasu, "Precision Measurment of x, Q^2 and A-Dependence of $R = \sigma_L/\sigma_T$ and F_2 in Deep Inelastic Scattering", PhD thesis (The University of Rochester, 1988).

[56] A. Aste, C. von Arx, and D. Trautmann, The European Physical Journal A - Hadrons and Nuclei **26**, 167 (2005).

[57] E. Kargiantoulakis, "A precision test of the standard model via parity-violating electron scattering in the Q_{weak} experiment", PhD thesis (University of Virginia, 2015).

[58] W. S. Duvall, "Precision measurement of the proton's weak charge using parity-violating electron scattering", PhD thesis (Virginia Polytechnic Institute and State University, 2017).

[59] J. P. Chen, H. Gao, T. K. Hemmick, Z. E. Meziani, and P. A. Souder (SoLID), (2014).